Dissertation

submitted to the
Combined Faculties for the Natural Sciences and for Mathematics
of the Ruperto-Carola University of Heidelberg, Germany
for the degree of
Doctor of Natural Sciences

Put forward by

Diplom-Physiker: Sebastian Schubert
Born in: Karl-Marx-Stadt, now Chemnitz

Oral examination: 11 December 2013

LineRESOLFT microscopy

Referees: Prof. Dr. Stefan W. Hell
Prof. Dr. Michael Hausmann

Abstract

Recent advances in RESOLFT (reversible saturable optical fluorescence transitions) microscopy have enabled the non-invasive three-dimensional visualization of numerous structures in living cells at high spatial resolution. This technique, which utilizes low light intensities, has manifold potential applications in the life sciences. The work presented here envisions further broadening the applications of RESOLFT microscopy by implementing a scheme for fast image acquisition of large fields of view, applicable to thick specimen.

With a pattern consisting of line-shaped intensity minima, this novel technique, called lineRESOLFT, permits fast imaging of living cells at ∼40 nm lateral resolution while offering strong optical sectioning. The full potential of this method is further illustrated by the achievement of continuous three-dimensional imaging of neurons in living brain slices with high spatio-temporal resolution, enabling the observation of rapid spine motility for large fields of view on the second time scale.

Zusammenfassung

Jüngste Fortschritte in der RESOLFT (reversible saturable optical fluorescence transitions) Mikroskopie haben die nichtinvasive, dreidimensionale Visualisierung einer Vielzahl von Strukturen in lebenden Zellen mit hoher räumlicher Auflösung ermöglicht. Die Technik, welche niedrige Lichtintensitäten nutzt, besitzt ein vielfältiges Anwendungspotential in den Lebenswissenschaften. Die hier vorgestellte Arbeit eröffnet neue Anwendungsmöglichkeiten der RESOLFT Mikroskopie, durch die Implementierung eines Systems zur schnellen Aufnahme von großen Bildbereichen, anwendbar für dicke Proben.

Mit Hilfe eines Musters bestehend aus linienförmigen Intensitätsminima, erlaubt diese neue Technik, genannt lineRESOLFT, eine schnelle Bildgebung von lebenden Zellen mit ∼40 nm lateraler Auflösung und einer deutlichen optischen Tiefenseperation. Das hohe Potential der Methode wird weiterhin durch eine kontinuierliche, dreidimensionale Bildgebung von Neuronen in lebenden Hirnschnitten mit hoher räumlich-zeitlicher Auflösung, welche die Beobachtung von schnellen Spinebewegungen für große Bildbereiche zulässt, verdeutlicht.

Contents

Chapter 1

Introduction

The foundations of far-field light microscopy were laid out by Ernst Abbe in 1873. He concluded that because of the wave nature of light, diffraction limits the resolving power of a microscope[1], with resolution being defined as the ability to distinguish close lying object details. Finding that only spatial frequencies up to a certain cut-off can be transmitted by an objective, focussed light always results in a blurred spot, known as the point spread function (PSF). Abbe found that the size of this spot, limited by diffraction, scales with the wavelength of light and inversely with the numerical aperture (NA) of the objective. This fundamental law is known as the Abbe diffraction barrier. Since the NA of a single objective, being the product of the refractive index of the lens and the sine of its semi-aperture angle, cannot be increased beyond the refractive index of the lens material (1.5 - 1.7), the diffraction barrier restricts the obtainable resolution of conventional microscopes utilizing visible light to about 200 nm in the focal plane and 500 nm along the optic axis.

However, increasing the aperture of a microscope was achieved with the invention of 4Pi microscopy[2,3]. Employing two opposing lenses, it doubles the solid angle available for the light illumination and/or collection. When operated with coherent illumination and detection, the axial resolution can be increased up to 7-fold[4,5]. Since the maximum aperture cannot be increased beyond the full spherical solid angle (4π), the wavelength of the light seemed to be the only parameter left for substantial improvement.

Hence, a straightforward way of obtaining higher resolution is utilizing light of a shorter wavelength. Unfortunately, the associated high photon energy might lead to pronounced photodamage. Additionally, optics for imaging with UV light below 350 nm

are demanding and expensive, since most lens materials are nontransparent for this wavelength range. However, X-ray microscopes have been successfully used to visualize structures of biological specimen[6,7]. Frozen, hydrated samples can be imaged with a resolution below 30 nm. Electron microscopes, based on the interaction of electrons with matter, provide even higher resolution. Featuring substantially shorter wavelengths, electron microscopy allows imaging with atomic resolution[8], making it a valuable tool to characterize the structure of inorganic and organic materials. However, applications to biological specimens are limited. Samples must undergo an extensive preparation process, possibly changing their cellular structure. Requiring fixed cells under vacuum conditions, this technique does not allow investigation of dynamic processes or cellular interactions. Furthermore, experimental restrictions in penetration depths prevent the imaging of thick specimen.

Another path to high resolution is to remove the fundamental far-field diffraction restrictions completely by applying near-field techniques. These methods rely on the rapidly decaying electromagnetic near-field and light has to be collected at close vicinity to the surface. In near-field scanning optical microscopy (NSOM), a fine tip consisting of a sub-wavelength-diameter aperture used for illumination or detection, is scanned across the surface, placed at a distance much smaller than the wavelength. Exploiting the properties of evanescent waves, resolution compared to the diffraction limited far-field microscopy can be 10-fold higher lateral and 100-fold higher axial[9]. Another scanning probe method, atomic force microscopy (AFM), records the topography of the surface by sensing forces between the tip and the surface with high sensitivity[10]. The disadvantage common to all these lens-less approaches is their bondage to surfaces. Their inability to research the interior of cells greatly restricts their usage in the life sciences.

1.1 Far-field fluorescence microscopy and the advent of fluorescence nanoscopy

In order to address biological problems, a non-invasive, three-dimensional visualization of living cells and their dynamics with high spatio-temporal resolution is desirable, preferably in the natural environment of biological specimens. Far-field fluorescence

microscopy best suits these challenging tasks. With the development of powerful labelling techniques, like antibody-based immunostaining[11] in the 1940s, displaying a high specificity, it was made possible to visualize virtually any protein with a high contrast. Nowadays, fluorescence microscopy is widely used in the life sciences and has become "an integral part of the basic toolbox of many biologists" [12].

The invention of confocal microscopy in 1961[13] is a major cornerstone of fluorescence microscopy. Point-like illumination and the introduction of a pinhole in front of the detector provide strong optical sectioning (see Section 3.1), whereas conventional bright-field microscopes suffer from an out-of-focus excitation resulting in an image blur. Thus, the possibility to reconstruct three-dimensional images of thick specimens has led to countless biological applications. In principle, when using an infinitesimal small pinhole, confocal microscopy additionally improves lateral resolution by a factor of two compared to the widefield case. Under experimental conditions, the choice of a finite pinhole size, determined by the need to collect sufficient signal, prevents such a strong improvement. However, cameras consisting of multiple detectors allow doubling of the lateral resolution without losing signal strength[14]. Another way of doubling the resolution without discarding any emission light was presented by the introduction of structured illumination microscopy (SIM)[15]. Instead of a point-like illumination, this widefield-based technique uses a pattern of parallel lines formed by standing waves. After shifting and rotating of the pattern, linear deconvolution reconstructs the image. While not sharing the strong optical sectioning strength inherent to confocal imaging, the parallel illumination of a large area requires less recording steps, thus facilitating a much faster image acquisition[16]. However, all those methods based on linear fluorescence response are fundamentally limited in their resolution[17].

Instead, recent developments[17–20] have established techniques to image well beyond the diffraction barrier, enabling an unprecedented spatio-temporal resolution[21]. These methods, called super-resolution far-field fluorescence microscopy or nanoscopy, offer theoretically unlimited resolution beyond the diffraction barrier and are based on fluorophores transiently populating distinct fluorescent states[17,22]. If two fluorescing molecules reside within a diffraction limited area, they can neither be excited nor detected separately. However, by sequentially switching them between fluorescent ("on") and non-fluorescent ("off") states, with one molecule being off while the other being on, they can be read out separately.

1. INTRODUCTION

The first concept to break the diffraction barrier was stimulated emission depletion (STED)[23,24]. Exploiting the photophysical properties of fluorophores, a part of the excited (on) molecules is sent back to their ground (off) state, preventing them from fluorescing. Typically, using a donut-shaped beam for this switching off consisting of a central intensity zero, the remaining on-molecules are located within an area much smaller than the diffraction-limited spot. Through a repeated coordinate-targeted preparation and read-out, accompanied by scanning the beams across the sample, a sub-diffraction resolution image is formed automatically. A resolution enhancement down to $\sim$20 nm with conventional organic dyes was demonstrated[25,26] and fluorescent nitrogen vacancies in diamond could be resolved with sub-10 nm resolution[27]. However, the de-excitation by stimulated emission requires high light intensities $> 10\,\mathrm{MW/cm^2}$. While it has been demonstrated to be compatible to live-cell measurements[21,28–31], methods applying low light levels and a low dose intake can minimize photodamage and reduce photobleaching.

Instead of inducing the on-off transitions at defined positions, stochastic nanoscopy techniques are based on switching the single-molecule fluorescence randomly in space. Invented in 2006, stochastic optical reconstruction microscopy (STORM)[18] and photoactivated localization microscopy (PALM)[19,20] localize individual molecules sequentially with very high accuracy. Operating in widefield mode, they cover a large area but temporal resolution suffers from the need to collect many frames[32]. This trade off is common to all single molecule localization methods, including techniques exploiting random fluctuations of the emitters[33,34]. However, recent developments in camera technology enabled much faster data acquisition[35]. Additionally, while using relatively low light intensities for switching, rapid localization requires high excitation intensities. Being a widefield technique the full sample is exposed to the illumination for the complete measurement, cumulating to a substantially high light dose intake.

Concurrent advances in photochromic genetically-encoded fluorescent proteins[36] that can act as endogenous labels, have opened new opportunities for high-resolution live-cell imaging. Reversible saturable optical fluorescence transitions (RESOLFT) nanoscopy[17,37], a coordinate-targeted switching technique, uses these proteins to achieve diffraction-unlimited resolution. Reversible switchable fluorescent proteins (rsFPs) that can be switched more than a thousand times have established RESOLFT nanoscopy as a powerful tool in the imaging of living cells with low light intensities and a low light

dose[38,39]. The initial point-scanning approaches used in this technique led to imaging times of 20-30 minutes for $\sim 10 \times 10\,\mu m^2$. More advanced rsFPs, exhibiting faster switching kinetics, reduced the recording time below one minute[40]. Still, the imaging speed for these point-scanning approaches remains mainly governed by the number of scanning steps.

However, the low light levels of RESOLFT facilitate the implementation of various parallelization schemes[41–43]. Combined with rapid data acquisition, fast live-cell nanoscopy of large fields can be achieved[43].

1.2 A route to fast, parallelized scanning nanoscopy

Parallelized scanning microscopy covering a large area was first provided by saturated structured illumination microscopy (SSIM)[44]. There, subdiffraction resolution is achieved by negative imaging. A sinusoidal excitation pattern saturates most of the fluorophores, leaving only those within a subdiffraction area in their off-state. Postprocessing the information contained in these dark regions renders the image. However, requiring high intensities, this technique is vulnerable to photobleaching. Furthermore, power limitations of available laser sources prohibit a versatile use of SSIM. For similar reasons, attempts to parallelize STED did not yet reach a large area coverage[45,46].

Nevertheless, RESOLFT, using $\sim 10^5$ times lower intensities, can overcome these power limitations. Recently, the application of RESOLFT to nonlinear SIM was successfully demonstrated[42]. While reaching a resolution comparable to point-scanning methods, the image acquisition was still slow. In another recently reported RESOLFT approach, a massive parallelization was achieved by switching off with two incoherently superimposed orthogonal standing waves[43]. The resulting multiple subdiffraction-sized foci of residual fluorescing molecules could be detected separately. A parallel read-out pushed down the imaging time below one second for a large field of view with sub-100 nm resolution. The common basis of these parallelization concepts is the simultaneous illumination of a large area, reducing the amount of required scanning steps. Thus, they feature similar characteristics to widefield microscopes. Consequently, while point-scanning RESOLFT offers strong optical sectioning making it suitable for three-dimensional imaging of thick tissue[47], parallelized widefield-based RESOLFT suffers from out-of-focus blur.

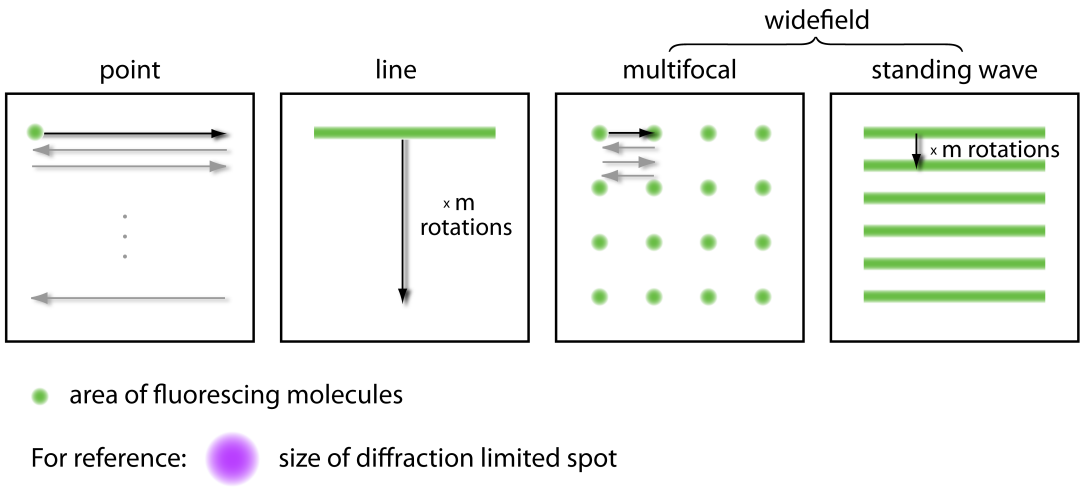

Figure 1.1: Scanning schemes in RESOLFT microscopy - Various scanning schemes offer different degrees of parallelization. While widefield based approaches offer massive parallelization, they miss the confocality inherent to point illumination. RESOLFT based on line illumination covers the middle ground, featuring substantial parallelization *and* optical sectioning.

In this thesis a novel parallelized RESOLFT implementation, based on line scanning[48–50] and therefore named lineRESOLFT, is presented. The technique bridges the gap between confocal schemes, which feature strong optical sectioning at the cost of long image acquisition times, and the widefield schemes, which feature fast imaging speed at the cost of background contamination. Fig. 1.1 illustrates various scanning schemes suitable for high resolution, coordinate-targeted RESOLFT and highlights the mediating character of line-based lineRESOLFT.

In order to reach a subdiffraction resolution d, the scan step size, according to the Nyquist-Shannon sampling theorem[51], has to be $\leq d/2$. Thus, to cover a square field of length l, point scanning needs $(2l/d)^2 \propto l^2$ steps. In contrast, the multifocal approach with a separation between the individual foci of at least the diffraction limit D, requires just $(2D/d)^2$ steps, independent of the field of view.

Line scanning covers the field by scanning only along one direction. Subsequent rotations and scans assure isotropic resolution. With $m \leq 10$ rotations being typically sufficient (see Section 2.1), it results in $(m \times 2l/d) \propto l^1$ steps, substantially speeding up image acquisition, as compared to the point scanning scheme.

The concept and realization of lineRESOLFT is explained in detail in Chapter 2.

It will be shown that using a switching-off illumination with line-shaped zeros enables parallel diffraction-unlimited resolution. The length of the line can be modified conveniently, thus readily adapting the degree of parallelization to the needs of the particular experiment.

Chapter 3 outlines the inherent confocality of the setup and derives the optical sectioning strength. The camera-based detection implementation allows an adjustment of the pinhole, from which an improvement of the sectioning over the confocal microscope can be achieved. For the first time it is demonstrated that this improved confocality is compatible with high NA objectives and subdiffraction resolution. Furthermore, the successful parallelization without impairing resolution is highlighted by imaging living cells with a lateral resolution $\sim$40 nm.

High spatio-temporal resolution imaging of neurons in living brain slices presented in Chapter 4, demonstrates the full potential of the method. Continuous optically sectioned recording allowed the investigation of the dynamics of distant spines with subdiffraction resolution and on the second-time-scale. For the first time, fast three-dimensional RESOLFT imaging of living tissue with subdiffraction resolution and a high degree of parallelization is achieved.

Chapter 2

Experimental methods and techniques

2.1 The lineRESOLFT microscope

2.1.1 Image formation

In a far-field fluorescence microscope the image is formed by collecting the photons emitted from the excited fluorophores with an objective lens. Once the photons are collected, the capability to spatially resolve structures in the resulting image is limited, caused by the diffraction of light [1].

Nanoscopy methods thus target on processes preceding the emission − the interaction of the fluorophores with the illumination light. Inducing transitions of the molecules between fluorescent and non-fluorescent states can enable the reconstruction of an image with theoretical unlimited resolution [17,22]. In RESOLFT, this switching can be spatially controlled (coordinate-targeted switching), while stochastic switching is used in STORM and PALM.

In the case of the lineRESOLFT microscope, the fluorophores are reversible switchable fluorescent proteins (rsFPs). Diffraction-unlimited resolution is achieved by the preparation of the rsFPs in two distinct states, a deactivated (off) or an activated (on) one. The ones in the deactivated state are not able to fluoresce, while the ones in the activated state absorb and emit photons like conventional fluorophores. Because each individual molecule can only either be on or off, the transition is saturable. Diffraction-unlimited resolution is achieved by spatially controlling the area of remaining activated

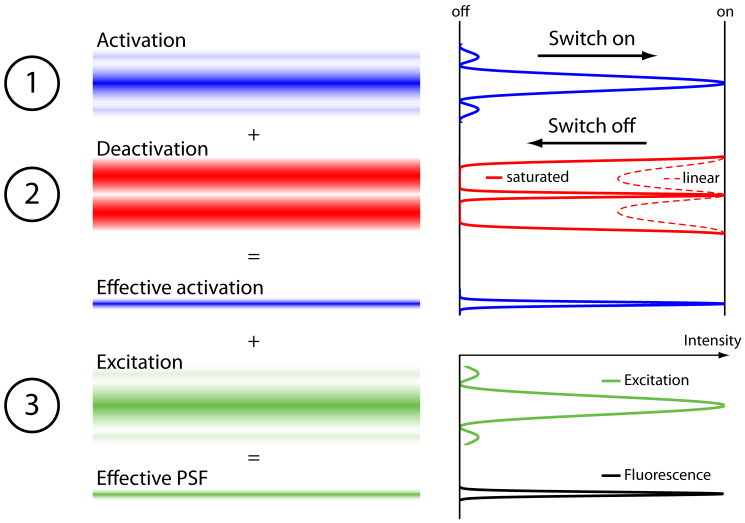

Figure 2.1: Parallelization in lineRESOLFT microscopy - Three line-shaped diffraction limited illumination pattern are used to prepare and excite the rsFPs. First, an activation beam switches them on. Second, most non-central rsFPs get switched off by a deactivation beam. Only the central activated molecules remain fluorescent (effective activation). Thus, subsequent excitation by a third beam leads to a subdiffraction sized effective PSF.

rsFPs. The following section explains in detail the methods and techniques used to gain this control.

2.1.1.1 Enabling parallel diffraction-unlimited resolution in 1d

Figure 2.1 illustrates the mechanism of reducing the area of activated fluorophores. A first illumination activates the rsFPs. A second illumination deactivates most rsFPs outside the central region where the intensity is zero. The probability to switch off a single rsFP (ideally) approaches 1 exponentially with an increase in irradiance. Thus, increasing the intensity or the duration of the deactivation shrinks the residual area of activated molecules. A third illumination excites the remaining activated rsFPs. The emitted photons are registered by a detector.

This sequence of activation, deactivation and excitation is then repeated while spatially moving the illumination intensity pattern over the sample. Registration of the detected fluorescence intensity with its corresponding pattern position allows reconstruction of a subdiffraction-resolved image.

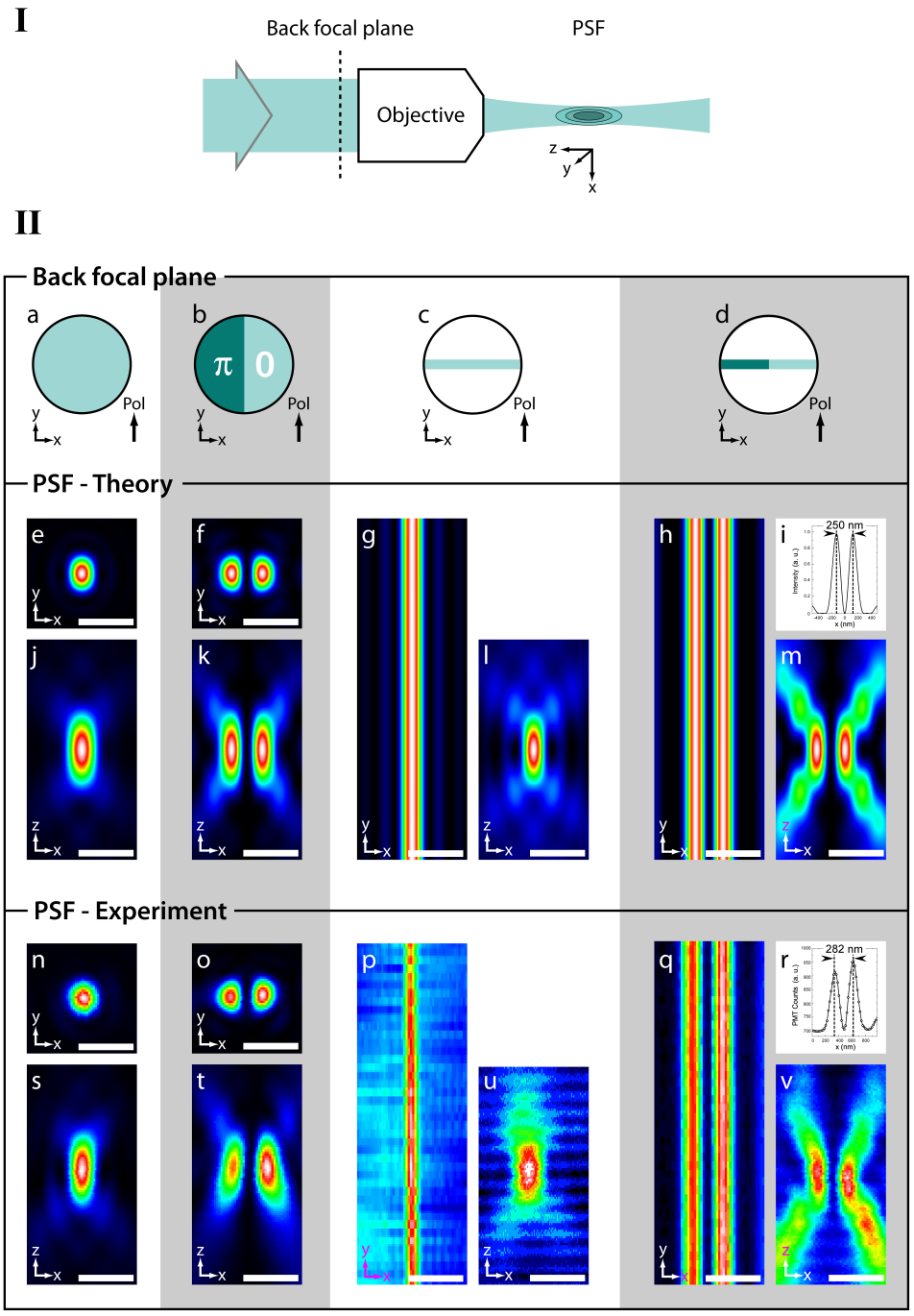

Figure 2.2: Illumination point spread functions - (**I**) Schematic illustration of the illumination. (**II**) **a-d**, Intensity, phase and polarization in the aperture of the objective lead to various PSFs in theory (**e-m**) and experimentally (**n-v**). The plots **i** and **r** show the intensity profiles orthogonal to the double lines in **h** and **g**.

Contrary to the typical spot scanning approach, line scanning is used. Hence the name lineRESOLFT. By illuminating all rsFPs along a line and detecting with a camera, the sample has to be scanned only orthogonal to the line in order to excite every molecule at least once. Subdiffraction resolution is achieved orthogonally for all pixel along the line, massively parallelizing the scanning. This parallelization vastly increases image acquisition speed. The structured line illumination is produced by under-filling the objective lens. Fig. 2.2 illustrates the under-filling and the resulting extension of the illumination PSFs. The pattern corresponding to point scanning are depicted in the two left columns, while the pattern corresponding to line scanning are shown in the two right columns. The PSFs were calculated (Fig. 2.2e-m) and measured (Fig. 2.2n-v) using light with a wavelength of $\approx 490\,\mathrm{nm}$ focussed by an 1.4 NA oil objective lens. The activation and excitation patterns (white rows) were produced with a beam of homogeneous phase while for the deactivation (grey rows) the phase of half of the beam is retarded by half a wavelength. This phase step leads to destructive interference in the center of the focal plane. The minimal intensity in this central area is called the "zero" of the PSF. Besides the quality and robustness of this zero, the steepness of the edge is crucial for experimentally achieving diffraction-unlimited resolution. The peak-to-peak distance (Fig. 2.2i,r) reaches down to $\approx 280\,\mathrm{nm}$ experimentally, outperforming deactivation pattern of grid scanning RESOLFT methods relying on point[38] or standing wave illumination[43]. Another important feature is the conservation of the confocality. When under-filling the objective, the length of the PSF in axial direction ($\approx \lambda$) remains mostly unchanged. Thus resolution in z is similar to a confocal microscope. Additionally the line microsccope achieves the parallelization of the scanning without losing the axial sectioning ability (see Section 3.1). Slightly disadvantageous are the stronger axial side lobes. But because the deactivation PSF has similar stronger side lobes, the additional activated rsFPs out-of-focus will get deactivated as well. Thus this mutually cancelling effects are, by continuing to restrict activated fluorophores to the focal plane, not impairing subdiffraction resolution.

Theoretical unlimited resolution orthogonal to the line is achieved by increasing the intensity or duration of the deactivation beam. This leads to a deactivation of all rsFPs except the ones close to the center of the line. Excitation of these remaining activated molecules leads to an effective line PSF whose thinness is not limited by diffraction but just by the practical feasibility of switching-off of only the non-central molecules.

2.1.1.2 Diffraction-unlimited resolution in all directions

A single, one-directional scan with the lineRESOLFT microscope achieves subdiffraction resolution orthogonal to the line, i.e. parallel to the scan direction. Having just to scan once along one direction speeds up the image acquisition time massively compared to point scanning where a second direction has to be scanned multiple times. In other words, the image acquisition time for a rectangular field of view of length l scales with l for the line scanning and l^2 for the point scanning approach. However, a single line scan improves resolution just in one direction.

For many applications one wishes to retrieve an image with subdiffractional resolved structures in any direction. The lineRESOLFT microscope accomplishes this by rotating and scanning the illumination PSFs in multiple directions. Each scan produces a high-resolved image containing details not visible in the others. A combination and subsequent deconvolution of all measurements results in an image with the highest content of structural details, exhibiting spatially isotropic resolution.

Acquiring several rotated images increases the total image acquisition time. Hence, a crucial question regarding speed is the number of required orientations which guarantee a certain resolution in any direction. The more orientations the better the guaranteed resolution.

To derive the relation between the number of orientations n and the guaranteed resolution $\lambda_{\min}$, we start with a single scan in one direction. Along this direction, imaging with subdiffraction resolution can be performed while the resolution orthogonal to it (i. e. parallel to the line) remains similar to the conventional diffraction limited widefield resolution. It is worth considering the situation in reciprocal (Fourier) space. The Fourier transform of the PSF is the optical transfer function (OTF). Its magnitude, called the modulation transfer function (MTF), determines the capability of the microscope to transfer spatial frequencies. Since any object can be described by Fourier theory as a superposition of basic waves, and fine details translate to waves with high frequency, high resolution manifests in an ability to transfer high spatial frequencies. Abbe[1] showed that because of diffraction, an objective with numerical aperture NA can only transfer frequencies lower than a certain value, called the cut-off frequency Λ_{co}. For light of wavelength λ, the MTF is zero for frequencies higher than:

$$\Lambda_{co} = \frac{2NA}{\lambda} \tag{2.1}$$

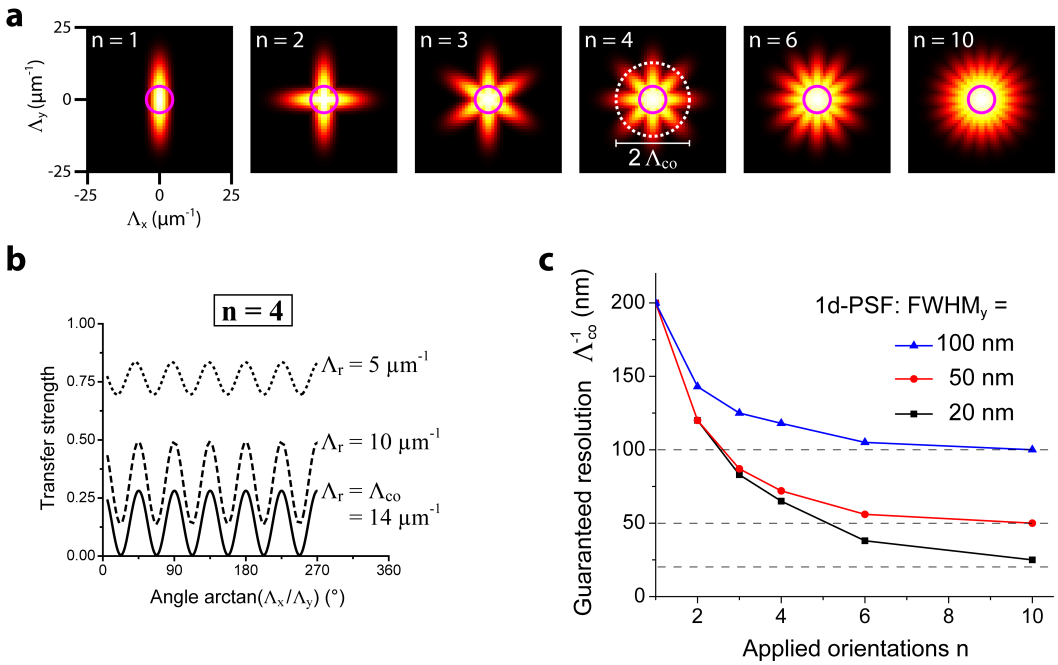

Figure 2.3: Support of the optical transfer function - (**a**) Combining several versions of the modulation transfer function (MTF) by consecutive imaging with rotated one direction (1d) subdiffraction-resolution PSFs increases the observable region of spatial frequencies; with the pink circle denoting the observable region for a widefield microscope. Without rotation, subdiffraction-resolution is only achieved along 1d. (**b**) Extending the circle of observation leads to a higher cut-off frequency Λ_{co}, defined as the maximum radius for which within the MTF does not reach zero. The plot shows the values of the MTF along its circumference. (**c**) This cut-off frequency increases with the number of orientations, ultimately reaching the maximum resolution equal to an isotropic subdiffraction-resolution PSF ($\mathrm{FWHM}_x = \mathrm{FWHM}_y$). The unrotated MTF (n = 1) in **a** corresponds to an effective 1d subdiffraction-resolution PSF of $\mathrm{FWHM}_y = 50\,\mathrm{nm}$).

Nanoscopy methods break this diffraction limit by enabling the transfer of higher spatial frequencies. In case of the lineRESOLFT microscope, this subdiffraction resolution is achieved only parallel to the scanning. Thus, when scanning in just one direction, the worst case (or guaranteed) resolution is $\lambda_{\min} = \Lambda_{co}^{-1} \approx 200\,\text{nm}$. The best resolution (parallel to the scanning) depends on the experimental conditions. In Fig. 2.3 an effective one direction (1d) subdiffraction-resolution PSF with $\text{FWHM}_y = 50\,\text{nm}$ is assumed. Panel 2.3**a** displays the support of the OTF. The extension over the circle of observation of a widefield microscope (pink circle) corresponds to an increased resolution for lineRESOLFT.

By rotating the PSF and scanning it along different directions, the goal is to eventually cover an isotropic area in Fourier space (Fig. 2.3a, $n = 10$). Upon increasing the number of orientations, every additional scan transfers some high spatial frequencies that were previously inaccessible. The circle of observation, guaranteeing the transfer of all frequencies laying within, gets extended. Its radius Λ_{co} is the reciprocal of the guaranteed resolution. It depends on the number of rotations as well as on the original effective PSF (Fig. 2.3c). As a rule of thumb, when starting with 50 nm resolution in one direction, three orientations already allow sub 100 nm resolution in any direction. With six orientations a resolution better than 60 nm is guaranteed.

However, this ideal treatment is only an estimate. Experimental conditions will cause further complications. First, the transfer strength of high frequencies is very low. Additionally, while low frequencies get transferred in several images, the highest frequencies will only appear in one. Thus noise will interfere with the resolution of the finest details. Second, the extent of the MTF may vary for different orientations. Hence, the initial resolution ($n = 1$) has to be estimated carefully for experimental conditions. With a too optimistic estimation one might use less rotations than actually required. The recording of some additional orientations in the experiment would automatically add a margin of safety.

In conclusion, the number of orientations required to achieve isotropic resolution is in the order of ten. For quasi-isotropic subdiffraction resolution below 100 nm as low as three orientations are sufficient. For a typical field of view of 20 x 20 μm^2, a point scanning nansocope with a step size of 20 nm uses $10^3 \cdot 10^3 = 10^6$ steps. The line scanning approach lowers the amount of steps to $\approx 10 \cdot 10^3 = 10^4$. Thus, the parallelization

ideally increases the image acquisition speed by two orders of magnitude. Larger fields of view would amplify the speed advantage of the lineRESOLFT microscope even more.

2.1.2 Experimental realization

The concept of lineRESOLFT, enabling parallelized diffraction-unlimited imaging, can be realized with any photocromic protein suitable for RESOLFT microscopy. Here, an implementation for negative-switching rsFPs was realized. Negative switching being defined as switching in which the excitation and deactivation wavelengths are the same. Fig. 2.4 depicts the setup which uses three separate laser beams – 405 nm for activation, 488 nm for deactivation and 491 nm for excitation.

The 491 nm light was provided by a diode-pumped solid-state laser (75 mW, Calypso, Cobolt). Its power was modulated by an acousto-optic modulator (AOTFnC-VIS-TN, AA Opto-Electronics). Linear, horizontal polarization was assured by passing it through a Glan-Thomson polarizer (B. Halle). A band-pass filter (BP2, z491/10, AHF Analysentechnik) spectrally cleaned the light. For spatial cleaning the beam was focused by an achromatic doublet ($f = 30$ mm, Qioptiq) onto a pinhole of 20 µm diameter and collimated (achromatic doublet, $f = 200$ mm, Qioptiq) back to a diameter of roughly 10 mm.

The light for the deactivation was provided by an Argon Ion laser (1.5 W, Innova 300, Coherent). After reducing the output power by a combination of a half-wave retardation plate and a Glan-Thomson polarizer (B. Halle), the light was guided to the optical table by a polarization-maintaining single-mode fiber (PMC-460Si-3.9N009-3-XPC-5000-P, Schäfter & Kirchhoff). After spectral filtering (BP1, z488/10, AHF) the power was controlled and stabilized by a laser power controller (LPC-VIS, Brockton Electro-Optics) and modulated by an acousto-optic modulator (MTS-110/A3-VIS, AA Opto-Electronics). Vertical polarization was guaranteed by a Glan-Thomson polarizer (B. Halle). For spatial cleaning the beam was focused by an achromatic doublet ($f = 40$ mm, Qioptiq) onto a pinhole of 20 µm diameter and collimated (achromatic doublet, $f = 200$ mm, Qioptiq) back to a diameter of roughly 10 mm. For phase retardation of half the beam a custom made phase plate (600 nm MgF_2 on glass, in-house built) was used.

The 491 nm and 488 nm light was combined using a polarizing beam splitter cube (PBS, PTW20 440 - 650 nm, B. Halle).

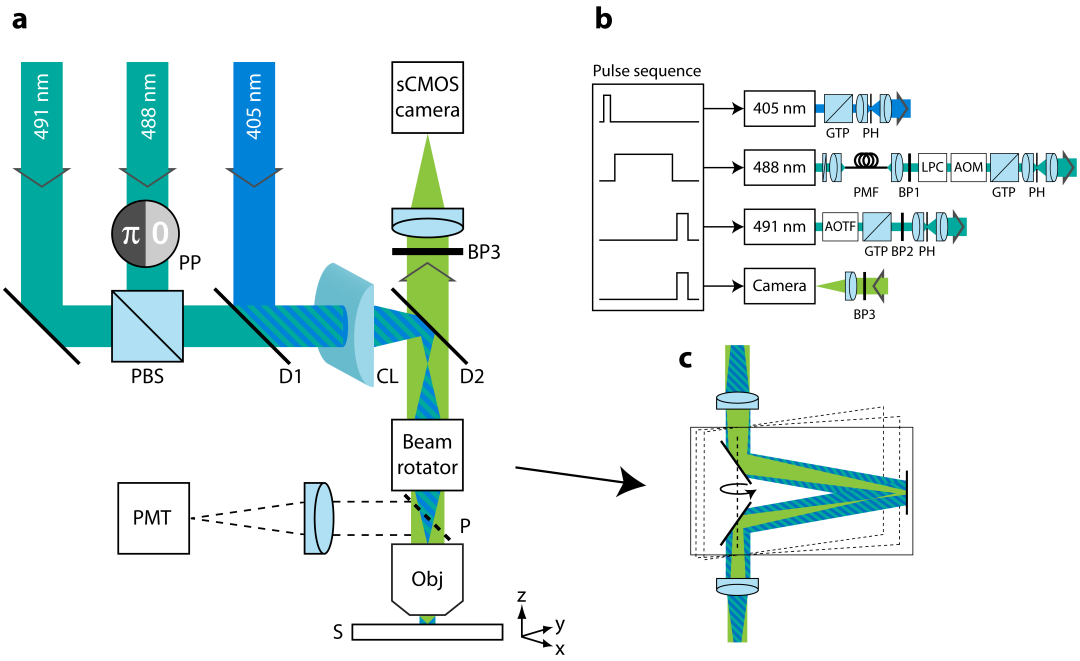

Figure 2.4: Schematic overview of the experimental setup - (**a**) Three laser beams, for activation (405 nm), deactivation (488 nm) and excitation (491 nm), are combined and a cylindrical lens (CL) focuses them to a line in the aperture of the objective (Obj). This translates into the extended illumination PSFs in the focal plane (see Fig. 2.2). The imprinted phase of 0-π (PP) causes the central intensity zero for the deactivation, leading to diffraction-unlimited resolution. The fluorescence is imaged on an sCMOS camera. (**b**) Illustration of the timing and power control as well as spatial and spectral cleaning of the beams. (**c**) A beam rotator enables isotropic diffraction-unlimited resolution by rotating the intensity pattern as well as the polarization and the phase.
AOM, AOTF: acousto-optic modulator; BP1-BP3: band pass filter; CL: achromatic cylindrical lens; D1, D2: dichroic mirror; GTP: Glan-Thomson prism; LPC: laser power controller; Obj: objective; P: pellicle; PP: 0-π phase plate; PBS: polarizing beam splitter; PH: pinhole; PMF: polarization-maintaining single-mode optical fiber; PMT: photomultiplier tube; S: sample on an xyz piezo stage

A continuous wave laser diode (405 nm, 60 mW, PhoxX, Omicron) was used for activation of the reversible switchable fluorescent proteins. Its output power was controlled and gated electronically. The beam, after passing a Glan-Thomson polarizer (B. Halle), was spatially cleaned by focusing with a fused silica UV-lens ($f = 50$ mm, Oerlikon) onto a pinhole of 20 µm diameter. After collimation by a fused silica UV-lens ($f = 300$ mm, LA4579-UV, Thorlabs) the activation beam was combined with the other two beams by a dichroic mirror (D1, zt405rdc, AHF).

A dichroic mirror (D2, 500dcxru, AHF) reflected all three beams into the aperture of the objective (HCX PL APO 100x/1.40-0.70 Oil CS, Leica Microsystems). Differently from confocal imaging, the lineRESOLFT setup under-illuminates the aperture of the objective in one direction in order to produce line foci in the focal plane. This was achieved by inserting an achromatic cylindrical doublet (CL, $f = 200$ mm, ACY254-200-A, Thorlabs). The superior aberration correction of the achromatic cylindrical lens compared to a cylindrical singlet allowed under-illuminating the aperture of the objective with a line thinness close to the diffraction limit ≈ 10 µm. This extended the full width half maximum (FWHM) of the PSFs to up to 70 µm in one direction (Fig. 2.5a,b) while conserving the diffraction limited FWHM for the unaffected direction (see Fig. 2.2p,u).

By temporary insertion of a pellicle (P, BP145B1, Thorlabs), the illumination foci were mutually aligned. The back scattered light from a silver nanobead (60 nm silver colloid, BBInternational) was focused onto a photomultiplier tube (PMT, MD 963, PerkinElmer). A pinhole or slit could be used to stop the light reflected from the coverslip from entering the detector. Secondarily the position of the phase plate was optimized this way. The quality of the central intensity minimum ("zero") of the deactivation beam was additionally confirmed by probing with a yellow-green fluorescent bead (20 nm carboxylate-modified FluoSpheres, Life Technologies), see Fig. 2.5c,d.

A beam rotator (K-mirror, home built) inserted into the beam path enabled rotation of the PSFs. It consists of three protected silver mirrors (PF10-03-P01, Thorlabs) mounted on a motorized rotation stage (8MR190-2-28 with 8SMC1-USB(h), Standa). Rotating the K-mirror by an angle β rotates the electromagnetic field by 2β. This enabled simultaneous rotation of the spatial intensity pattern of the beams as well as their polarization and phase. Additionally, two lenses ($f = 200$ mm and $f = 250$ mm, Qioptiq) worked as a 4f-relay. The fluorescence from the sample was collected by the same

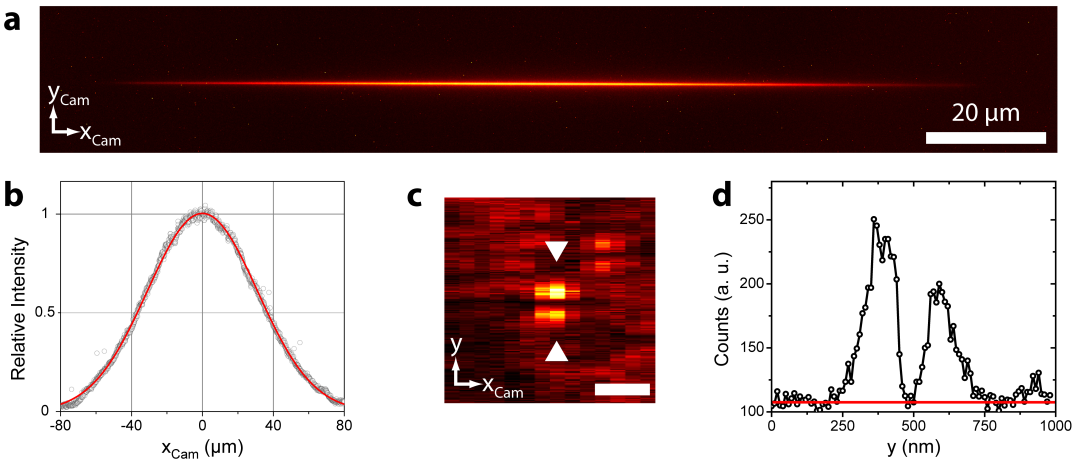

Figure 2.5: Dimensions of the illumination PSFs - (**a**) Excitation of a fluorescent membrane. (**b**) The size of the excitation PSF along x shows an extension to ∼73 µm (FWHM). (**c**) Scanning a 20 nm fluorescent bead along y while illuminating with the deactivation PSF demonstrates the quality of the zero (line profile in **d**). Scale bars: 20 µm (**a**) and 500 nm (**c**).

objective as used for illumination. After passing a band pass filter (BP3, HQ532/70, AHF) an achromatic doublet (f = 120 mm, Qioptiq) focused the fluorescence onto a scientific complementary metal-oxide semiconductor (sCMOS) camera (pco.edge, PCO AG). Because the fluorescence was sent through the beam rotator in the opposite direction, it was rotated back so that it would always hit the same lines of the camera, independent of the rotation of the illumination. Imaging with any arbitrary orientation of the line PSF was thus achieved without having to rotate the camera. The design of the sCMOS sensors makes the read out rate independent from the number of pixels along a line, leaving only the number of lines as the determining factor. Having just to read out a few central camera lines facilitates dwell times down to a few hundred microseconds.

A three-axes piezo stage (NanoMax MAX311D/M with BPC303, Thorlabs) positioned and scanned the sample. ImSpector, a software for data acquisition and analysis (in-house built), was used to control the measurements. Together with the help of a data acquisition card (NI PCIe 6353, National Instruments) it generated the scan voltages and triggered the start of the pulse sequence. The sequence, i. e. start and duration, was generated by a digital delay pulse generator (Model 9514, Quantum Composer)

which modulated the three laser beams and triggered the exposure of the camera. To assure the accuracy of the sequence, the pulses were monitored by a four channel digital real-time oscilloscope (TDS694C, Tektronix). The camera frames were recorded using the Camera link interface (microEnable IV VD4-CL, Silicon Software).

Custom MATLAB programs rendered the information of the raw data stacks into conventional (two-dimensional) images either by just displaying the central camera line adjusted for the scan position or by using more sophisticated algorithms, adjusting for background or out-of focus light or combining structural information of different PSF orientations.

2.2 Beam rotation

Having a non-isotropic effective illumination requires rotation when targeting for improved resolution in all directions. The lineRESOLFT microscope with its linear illumination PSFs uses a three mirror arrangement called K-mirror for its beam rotation.

2.2.1 Comparison of prism and mirror rotators

On-axis rotation is a common problem in optics and systems for beam rotation have been reported already several decades ago[52,53]. Because of manufacturing precision and reliability, most of them, e.g. Dove prism, Schmidt/Delta prism or Abbe prism, are based on glass prisms using total internal reflection.

Unfortunately, while relatively easy to manufacture, the implementation of these prisms has the inherent disadvantage of introducing aberrations at the glass-air interface, caused by refraction when entering and exiting the prism. If the propagation of the light is non-perpendicular to the front or back surface of the prism, the light gets refracted. The dispersion of the glass will then lead to chromatic aberrations.

This was tried to be circumvented by only using surfaces perpendicular to the propagation of the beam (Abbe type prism[52,54]). While this works well for rotating the collimated illumination in a conventional microscope, using these prisms to rotate the collected fluorescence would introduce the aforementioned aberrations. For infinity corrected objectives, the collected fluorescence of the focal plane consists of a superposition of several collimated waves of different propagation angles that in the end are

interfered to form the image. When passing the surface of a prism these different propagation angles would be responsible not only for chromatic aberrations of the typically broad-spectral fluorescence but the slightly different refraction for each angle would additionally lead to a distortion of the image. In case of the lineRESOLFT microscope, the use of non-collimated illumination beams add to the complications. The cylindrical lens placed before the beam rotator changes the propagation direction of the rays, focussing them in a line. Thus a spatially varying refraction at the air-glass interface of a prism beam rotator would then lead to astigmatism. Additionally, the lineRESOLFT microscope requires the preservation of the linear polarization of the deactivation beam.

That is why we opted for a mirror arrangement for the beam rotation. With the K-mirror, as used in modern telescopes[55], we were able to aberration-free rotate the intensity pattern, phase and polarization of the beams collinearly. The fluorescence was sent back the same path. By passing the rotator in the reverse direction it was de-rotated back to hit the same position on the camera, independent of the rotation. This was the key to achieve high read-out rates up to 2 kHz.

2.2.2 Theory of the K-mirror

The name K-mirror is derived from the shape of the mutual positions of the three mirrors. Their configuration is depicted in Fig. 2.6a. An image passing it gets inverted, and rotated double the rotation of the K-mirror.

The centers of the mirrors form a plane, which can be rotated to any angle β. Their surfaces are perpendicular to that plane. A ray entering the K-mirror collinear to the axis of rotation hits the first mirror M1 in P_0 and gets reflected to the mirror M2 whose surface is parallel to the axis of rotation. From that surface it gets reflected back to the third mirror M3 which reflects it out of the K-mirror. The angles of M1 and M3 are chosen so that the exiting ray is collinear with the entering one. This determines the length l and height h of the K-mirror.

Let $\vec{P_0} = (0,0)^T$ be in the center of the coordinate system. A second ray enters the K-mirror under a small angle $\vec{\epsilon} = (\epsilon_x, \epsilon_y)^T$, with ϵ_x and ϵ_y being the projections to the plane defined by the axis of rotation and the x- or y-axis, respectively. It hits M1 offset in $\vec{P} = (x,y)^T$. Let us further assume that M3 has a small angular shift of $\vec{\delta} = (\delta_x, \delta_y)^T$, with δ_x and δ_y being the projections into the rotated K-mirror plane, representing an internal angular misalignment of the whole K-mirror. Replacing the

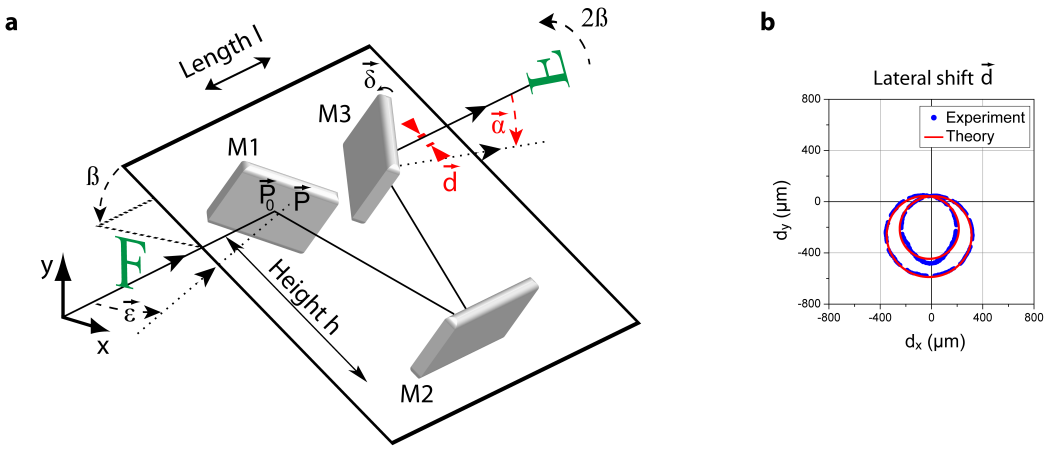

Figure 2.6: K-mirror - (**a**) Detailed description of the K-mirror arrangement and possible misalignment deviations. An image passing the K-mirror gets rotated and inverted along the y-axis. Rotating the K-mirror by β results in an image rotation of 2β. (**b**) Under continuous rotation a misaligned K-mirror leads to characteristic trajectories of the lateral shift of the outgoing ray with respect to the incoming ray.

offset of M3 by a misalignment of M1 or M2 is straightforward. With these deviations the second ray is reflected differently from the first (optimal) ray. Its exit will not be identical with the axis of rotation. It will hit M3 by an offset $\vec{d}$ and exit under an angle $\vec{\alpha}$. With that we derive the following equation for the spatial exit offset:

$$\vec{d} = \underbrace{MR_{2\beta} \cdot \vec{P}}_{\text{rotation and inversion}} + \underbrace{R_\beta^{-1} A R_\beta \cdot \vec{\epsilon}}_{\text{rotation axis tilt}} + \underbrace{2hR_\beta^{-1} \cdot \vec{\delta}}_{\text{internal misalignment}} \tag{2.2}$$

with the *rotation matrix*

$$R_\beta = \begin{pmatrix} \cos\beta & -\sin\beta \\ \sin\beta & \cos\beta \end{pmatrix},$$

the *mirror matrix*

$$M = \begin{pmatrix} 1 & 0 \\ 0 & -1 \end{pmatrix}$$

and the *alignment matrix*

$$A = \begin{pmatrix} \sqrt{4h^2 + l^2} & 0 \\ 0 & 2h \end{pmatrix}.$$

The displacement consists of three terms. The first term describes the feature of rotating the beam, while the other two are deviations caused by a misalignment of the

K-mirror.

The first term reveals that an image passing the K-mirror gets rotated by 2β. This constitutes the ability of the K-mirror to rotate the beam. Additionally the image gets inverted along one axis. When working with elliptically polarized beams, this leads to a reversing in handedness, optionally resolved by adding a half-wave plate.

The second term is caused by the axis of rotation not being parallel to the propagation of the beam. A decomposition of this angular deviation in two parts, one parallel to the plane of the K-mirror and the other one orthogonal to it, reveals that the displacement is the product of each part with its corresponding travel distance through the K-mirror.

The third term represents an internal misalignment of the mirrors. Here the displacement does not depend on the position or angle of the incoming ray. Instead a constant displacement proportional to the height h of the mirror and the internal angular misalignment is added, its vectorial composition depending on the angle of rotation.

2.2.3 Alignment of the K-mirror

Passing a ray under continuous rotation of the K-mirror and monitoring the displacement at its exit results in characteristic curves, called limaçons Fig. 2.6b.

A limaçon[56], the special case of an epitrochoid, is produced by tracing a point fixed to a circular wheel as the wheel rolls along on top of another circular wheel with the same radius. In case of the K-mirror, the two "wheels" are introduced by the internal mirror misalignment rotating on top of the external lateral or angular misalignment of the rotation axis with respect to the ray axis.
The lineRESOLFT microscope requires the lateral shift of the outgoing beam with respect to the incoming beam to be smaller than 5% of the aperture of the objective ($\approx$ 280 µm) and the parallelism to be better than 1 mrad ($\approx$ 2 µm shift in sample space). The restrictions arise from the necessity to preserve the zero of the deactivation PSF and the field of view for multiple angles.

For matching these tight requirements, we developed a protocol for aligning the K-mirror. Two position sensitive diodes (PSDs) tracked the trace of a ray sent through the rotating K-mirror. Knowing the distances of the PSDs from the K-mirror, we could calculate the curves of the lateral and angular displacements at the exit mirror. With

a self-written Matlab code we were able to fit the measured curve and with help of Eq. 2.2 derived the (mis)alignment parameters $\vec{P}$, $\vec{\epsilon}$ and $\vec{\delta}$.

Reducing the fitting time to below one second, enabled tracking of the ray trajectory while simultaneously deriving the parameters. This allowed us to continuously minimize the misalignment. The necessary degrees of freedom were provided by placing the mirrors on kinematic mounts and mounting the whole K-mirror on a 4-axes stage, consisting of a 2-axes tip-tilt stage (Edmund Optics) and a 2-axes lateral stage (Newport).

Because for continuous rotation Eq. 2.2 leads to curves that are ambiguous with respect to the alignment parameters, we introduced known misalignments in the beginning of the alignment process. Combining the measured curves with that a priori knowledge led to definite parameters $\vec{P}$, $\vec{\epsilon}$ and $\vec{\delta}$, which then were minimized.

With the help of this alignment procedure we pushed down the shifts for a full turn of the K-mirror to less than 50 µm in the lateral and less than 0.1 mrad ($\approx 2'$) in the angular direction (Fig. 2.7). Considering that for the lineRESOLFT microscope a half turn of the PSF covers the full sample space, means that already a quarter of a turn of the K-mirror is sufficient and yields even smaller deviations during the imaging process.

Repeating the measurements after three days revealed no significant change in alignment.

Exceeding the requirements for the rotation by a wide margin and confirming the stability towards drift, the K-mirror is a robust and reliable tool for aberration-free rotation of the beam, polarization and phase.

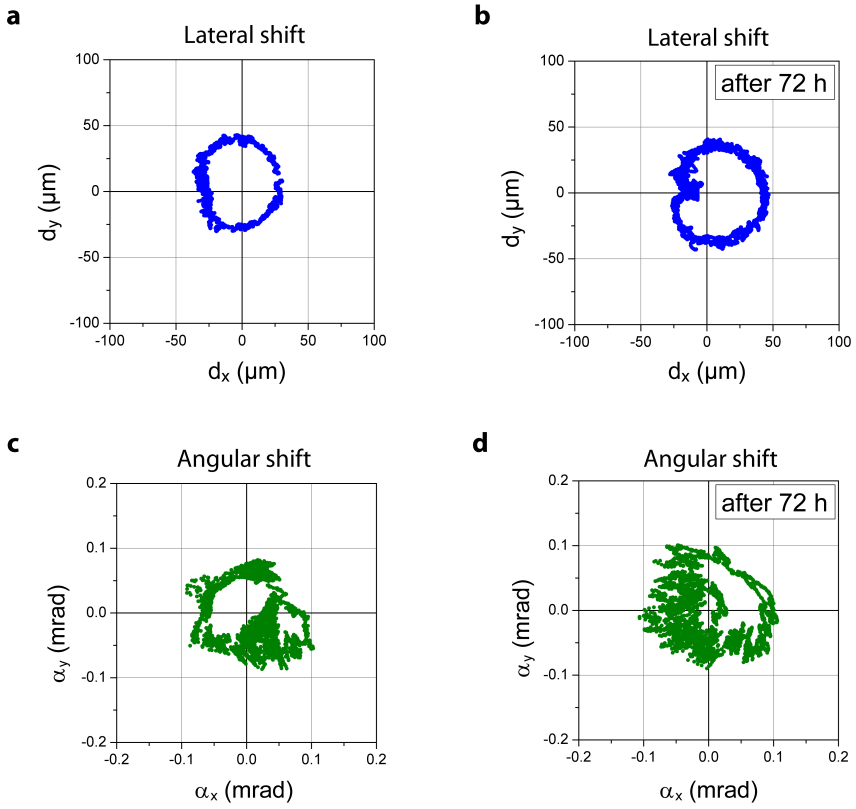

Figure 2.7: Residual deviations after full alignment - Lateral (**a**,**b**) and angular (**c**,**d**) residual shift for continuous rotation after full alignment. Measuring the identical configuration 72 h later confirmed the time stability of the K-mirror (**b**,**d**).

Chapter 3

Performance of the microscope

3.1 Optical sectioning strength

Besides resolving power, the ability to block out of focus light is a typical measure of performance in a microscope. In a confocal microscope this is achieved by illuminating the sample with a point source and introducing a pinhole in front of the detector, letting only pass the light originated in focus. Other methods such as multiphoton excitation microscopy[57,58], 4Pi microscopy[2,59], total internal reflection fluorescence (TIRF) microscopy[60,61] or selective plane illumination microscopy (SPIM, also known as Light Sheet Microscopy)[62] achieve improved optical sectioning by confining the excitation of molecules to the focal plane.

The extended illumination pattern in one direction in the lineRESOLFT microscope boosts the imaging speed significantly but comes at the cost of exciting a broader area, in *and* out of focus. Detecting the fluorescence with single pixelated line detector would therefore reduce the optical sectioning strength compared to the confocal case. This can be overcome by detecting with multiple line detectors, parallel to each other. A detector shifted away laterally from the central illumination maximum would not detect the in focus light anymore but still register the fluorescence from out of focus illumination. Subtracting this fluorescence from the signal of the central detector gives rise to an improvement in optical sectioning strength from z to z^3. For the case of objectives with low numerical aperture this has been demonstrated before[63]. We extended this method to high NA objectives and employed it in the lineRESOLFT microscope featuring multiple illumination lines.

In this chapter the improved sectioning strength is demonstrated in detail and it is shown that the suppression of far from focus signal even surpasses the confocal case.

3.1.1 Derivation of the infinite plane response

While the resolving power of a microscope is characterized by the response to a point, optical sectioning strength is measured by the response to an infinitely thin fluorescent sheet parallel to the optical axis, called *infinite plane response (IPR)* or *z response*. Mathematically this thin layer is expressed by a Dirac delta function

$$Obj(x,y,z) = \delta(z-\tilde{z}) = \begin{cases} +\infty, & z = \tilde{z} \\ 0, & \text{otherwise} \end{cases}$$

The detection point spread function of a small pixel is approximated by a two dimensional Gaussian

$$Det(x,y,z) = \frac{1}{2\pi\sigma^2}\exp\left(-\frac{x^2+y^2}{2\sigma^2}\right), \text{ with } \sigma = \sigma(z) \tag{3.1}$$

as well as the line excitation extended in the x-direction

$$Exc(x,y,z) = \frac{I_0}{2\pi\sigma\sigma_{ext}}\exp\left(-\frac{x^2}{2\sigma_{ext}^2}-\frac{y^2}{2\sigma^2}\right), \text{ with } \sigma_0 = \sigma(0) \ll \sigma_{ext}(0). \tag{3.2}$$

For simplification a negligible Stokes shift is assumed ($\lambda_{Exc} \approx \lambda_{Det}$).
The broadening of the PSF for defocus is[64]

$$\sigma(z) = \sigma_0\sqrt{1+\left(\frac{z\lambda}{4\pi\sigma_0^2}\right)^2}. \tag{3.3}$$

Image formation in a fluorescence microscope is a convolution ($\otimes$) of the detection with the excited object. Assuming linear, unsaturated excitation yields:

$$Image = (Object \cdot Excitation) \otimes Detection$$

For a detector centered in the corresponding sample coordinates $\boldsymbol{r} = (x_0, y_0, z_0)$ placed in focus $z_0 = 0$, the infinite plane response IPR is thus

$$IPR(x_0,y_0,0) = \frac{I_0}{4\pi^2\sigma^3\sigma_{ext}}\iint_{\mathbf{R}^2}\exp\left(-\frac{x^2}{2\sigma_{ext}^2}-\frac{y^2+(x-x_0)^2+(y-y_0)^2}{2\sigma^2}\right)\,\mathrm{d}x\,\mathrm{d}y$$

which can be simplified to

$$IPR(x_0,y_0,0) = \frac{I_0}{\sigma\sqrt{2(\sigma^2+\sigma_{ext}^2)}}\cdot\exp\left(-\frac{x_0^2}{2(\sigma^2+\sigma_{ext}^2)}-\frac{y_0^2}{4\sigma^2}\right). \tag{3.4}$$

Now the sectioning strength can be derived. Considering the confocal case, where $\sigma_{ext} = \sigma$, the intensity for the central detector is

$$IPR_{conf} \propto \sigma^{-2} \approx const. \cdot \tilde{z}^{-2}, \qquad \text{for } |\tilde{z}| \geq 4\lambda.$$

In case of the line microscope, according to Eq. 3.3 $\sigma^2 + \sigma_{ext}^2$ can be treated as a constant for the relevant region $|\tilde{z}| \leq 10^4\lambda$. The intensity for a detector in the central line ($y_0 = 0$) is

$$IPR_{line} \propto \sigma^{-1} \approx const. \cdot \tilde{z}^{-1}, \qquad \text{for } |\tilde{z}| \geq 4\lambda.$$

Summarizing this equations in the context of experimental conditions leads to the conclusion that the residual intensity originating from a defocused infinitely thin fluorescent sheet drops with $defocus^{-2}$ in the confocal case. This strong decline is partly lost in the line microscope. Here the drop follows the $defocus^{-1}$. Extending the excitation to all directions leads to widefield illumination where the discrimination is lost completely. Thus for a conventional widefield microscope holds:

$$IPR_{widefield} = const.$$

3.1.2 Differential detection for the line microscope

To obtain an improved sectioned image a differential detection (DD) is used. For this, the signal from a detector shifted Δy orthogonal to the central line gets subtracted, hence the name *differential* detection. This results in a plane response of

$$\begin{aligned} IPR_{line,DD} &= IPR(x_0, 0, 0) - IPR(x_0, \Delta y, 0) \\ &\propto \sigma^{-1} \left[1 - \exp\left(-\tfrac{(\Delta y)^2}{4\sigma^2}\right)\right] \end{aligned} \tag{3.5}$$

Taylor expansion leads to

$$IPR_{line,DD} \approx const. \cdot \tilde{z}^{-3}, \qquad \text{for } |\tilde{z}| \geq 4\lambda. \tag{3.6}$$

The differential detection strongly suppresses far from focus light. The residual detected intensity drops with $defocus^{-3}$, resulting in a superior optical sectioning strength compared to the confocal microscope.

Some consideration must be given to choosing the shift Δy of the second detector. The smaller the shift the better the optical sectioning close to the focal plane. Nevertheless, it is undesirable to lose signal that originated from in focus specimen, resulting

in a reduced signal to noise ratio (SNR). Additionally, a bright structure located close to the shifted detector could negate the detection of a dimmer structure located close to the central detector, potentially resulting in negative values. The in-focus signal drop orthogonal to the illumination line can be estimated by Eq. 3.2:

$$Signal_{in-focus} \propto \exp\left(-4\ln 2\,\frac{y^2}{FWHM^2}\right), \tag{3.7}$$

corresponding to a signal drop below 5% for $y \geq FWHM$.

In conclusion, placing the differential detector $2 \cdot FWHM$ apart from the central detector limits negative values to 5% of the maximum count. Averaging the signal from the differential detector with a third detector, shifted the opposite direction ($-\Delta y$), does further reduce the negative values by a factor of ≈ 2.

Because of the reduced FWHM of the effective illumination in RESOLFT microscopy, we regularly targeted for a shift equal to a drop below 10^{-3}. Possible remaining negative values were set to zero.

3.1.3 Experimental demonstration

Probing the sectioning strength was realized by measuring the fluorescence intensity of a thin supported lipid bilayer (<10 nm) labeled with Oregon Green. By detecting with a camera array of 16 lines, conventional and differential detection were recorded simultaneously, eliminating the possibility of artefacts.

Fig. 3.1 shows the obtained dependency of the normalized intensity over defocus. Experimental data is compared to the theoretical behavior of the widefield, line and confocal microscope. The theoretical curves were calculated using Matlab programs combined with in-house developed routines for calculating the illumination and detection PSFs. The finite size of the camera pixel was taken into account.

The suppression of out of focus light matches the theoretical predictions. Confining the illumination to a smaller focal area improves optical sectioning. While line illumination improves the widefield microscope, it lags behind the point source illumination of the confocal microscope. Employing the differential detection extricates the line microscope from this limitation, improving the sectioning strength over its confocal counterpart. The steeper decline suppresses most of out of focus light, resulting in an improved contrast in thick samples.

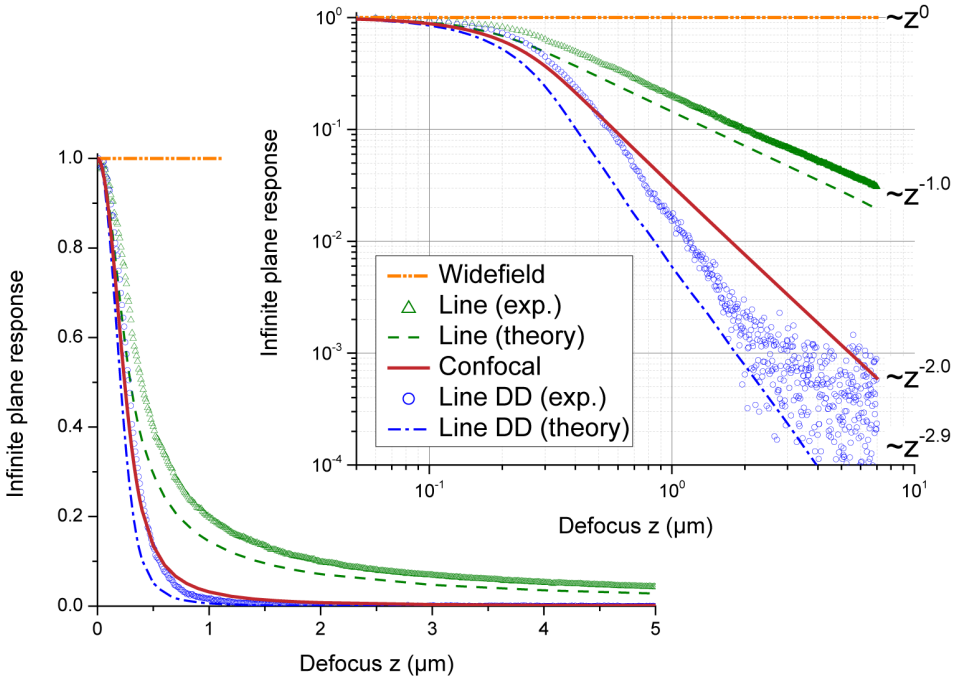

Figure 3.1: Infinite plane response - The plots demonstrate the optical sectioning strength by showing the intensity drop when defocussing a thin fluorescent sheet. Left: linear scales, Right: double logarithmic. Comparing widefield, line and confocal excitation yields an asymptotic defocus dependence in the order of magnitude of 0, -1 and -2, respectively. Applying the differential detection (DD) to the line microscope improves the sectioning strength significantly, suppressing out of focus light even more than in the confocal microscope.

The small deviation between experimental data and the theoretical model can be attributed to imperfect experimental conditions like small aberrations of the PSFs. As signal drops in regions of very low signal-to-noise ratios, it gets impossible to discriminate noise from signal.

An asymptotic decline to $defocus^{-2.9}$ for the differential detection matches the low NA behavior reported before[63]. Demonstrating that this steep decline is not limited by the NA allowed us to merge the improved sectioning strength of differential detection with the much better resolution of high NA objectives.

3.1.4 Differential detection lineRESOLFT in living cells

The preceding considerations focussed on a common line microscope, with the excitation being the only illumination. As was shown, line excitation already results in a strong sectioning. The lineRESOLFT case, using three line illuminations, is thus expected to at least match this behavior. In order to demonstrate the compatibility of the differential detection (DD) with the lineRESOLFT microscope, a three-dimensional image of a living cell (HeLa) was acquired. Fig. 3.2 displays an xz-slice through the cell, visualizing a part of the cytoskeleton, being a dense filamentous network. Applying the differential detection to the lineRESOLFT microscope greatly improves the axial sectioning. Comparing conventional and differential detection proves the strong reduction of out of focus light detection.

While differential detection does not increase the cut-off frequency of the microscope's optical transfer function but solely enhances contrast, it still boosts the ability to discriminate structures axially close to each other under experimental conditions, i.e. with finite signal-to-noise ratios Fig. 3.2*c*. Defining resolution as the ability to discriminate structures close to each other, differential detection leads to an increased axial resolution in raw data.

In conclusion, lineRESOLFT DD is a highly competitive tool for measuring thick samples, providing both *parallelization* and *confocality*. By subtracting out of focus light, background gets suppressed resulting in a clear signal originated in-focus. Three-dimensional imaging shows axial resolution comparable to a confocal microscope while having a better optical sectioning capability.

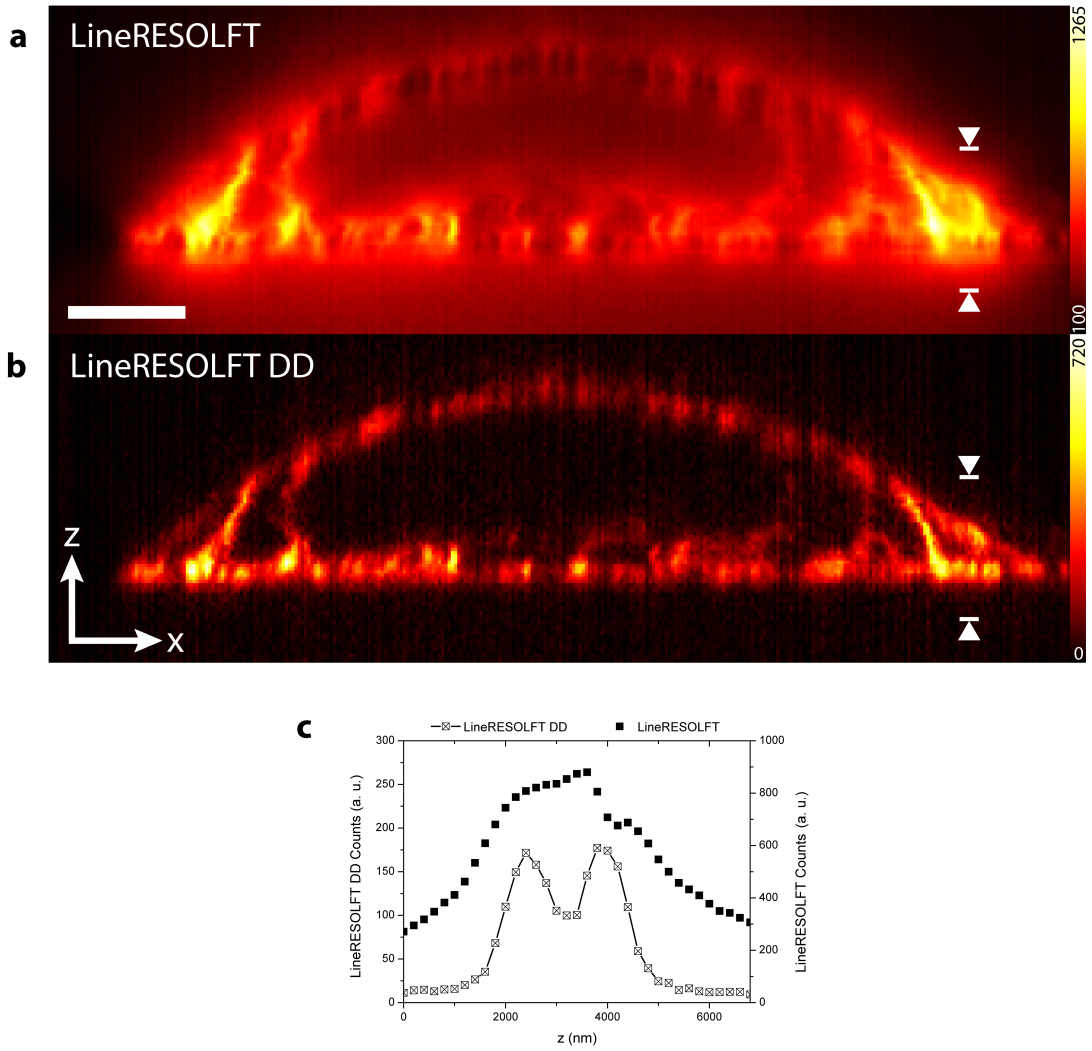

Figure 3.2: Optical sectioning in the lineRESOLFT microscope - An xz-slice of a living HeLa cell expressing keratin-19−rsEGFP(N205S) imaged in lineRESOLFT mode with conventional (**a**) and differential (**b**) detection (DD). The slice is retrieved from a full xyz-data stack of 43.52 µm x 18 µm x 14 µm by averaging over 180 nm along y. When applying the differential detection a strong improvement in signal-to-background facilitates the discrimination of otherwise unresolved structures (**c**). The arrows in **a** and **b** indicate the positions and widths of the 8-pixel wide average line profiles in **c**. Scale bar: 5 µm

Using unsaturated activation and excitation would further enhance the sectioning strength in RESOLFT. If fluorescence requires two steps, activation and excitation, it essentially becomes a two-photon process, without need to double the wavelength. This increases axial resolution and reduces out-of-focus fluorescence. For bright samples the unsaturated activation and excitation resulting in a reduced signal is a valuable trade-off in exchange for an additional gain in sectioning strength. Deconvolution, using the information of several parallel camera lines, would further render subtraction unnecessary and strengthen the optical sectioning even more. However, detailed a priori knowledge, like the shape of the effective PSF, is necessary, making deconvolution less robust.

3.2 Resolving power in the focal plane

3.2.1 Resolution enhancement along the scanning direction

The resolving power of the lineRESOLFT microscope is best verified when imaging under realistic conditions, i.e. in living cells or tissue. Inherently, the line PSF best suits imaging of thin, linear filamentous structures.

Keratin, a family of fibrous structural proteins, forms intermediate filaments, one of the three main kinds of filaments that compose the cytoskeleton of eukaryotic cells (Fig. 3.3). A living mammalian cell, kidney epithel cell of *Potorous tridactylis* (PtK2), was imaged multiple times with the lineRESOLFT microscope. A broadened excitation as well as saturated activation and excitation resembled conventional widefield imaging (Fig. 3.3a). Turning on the deactivation beam enabled subdiffraction resolution along the vertical scan direction (Fig. 3.3b). Clearly, filaments that are not resolved in conventional microscopy become separable when employing lineRESOLFT (Fig. 3.3c,d). Displayed are raw data without any correction or post-processing. A single scan allowed imaging a large field of view (FOV). Over the full horizontal extent of 57 µm the line PSF provides homogeneous illumination. Using saturated activation and excitation prevents the fluorescence intensity to drop off at the edges, maximizing it over the full FOV. To prove that the resolution enhancement is observed over the whole FOV, line profiles of distant filaments are displayed (Fig. 3.3d,i), showing similar widths < 60 nm (FWHM).

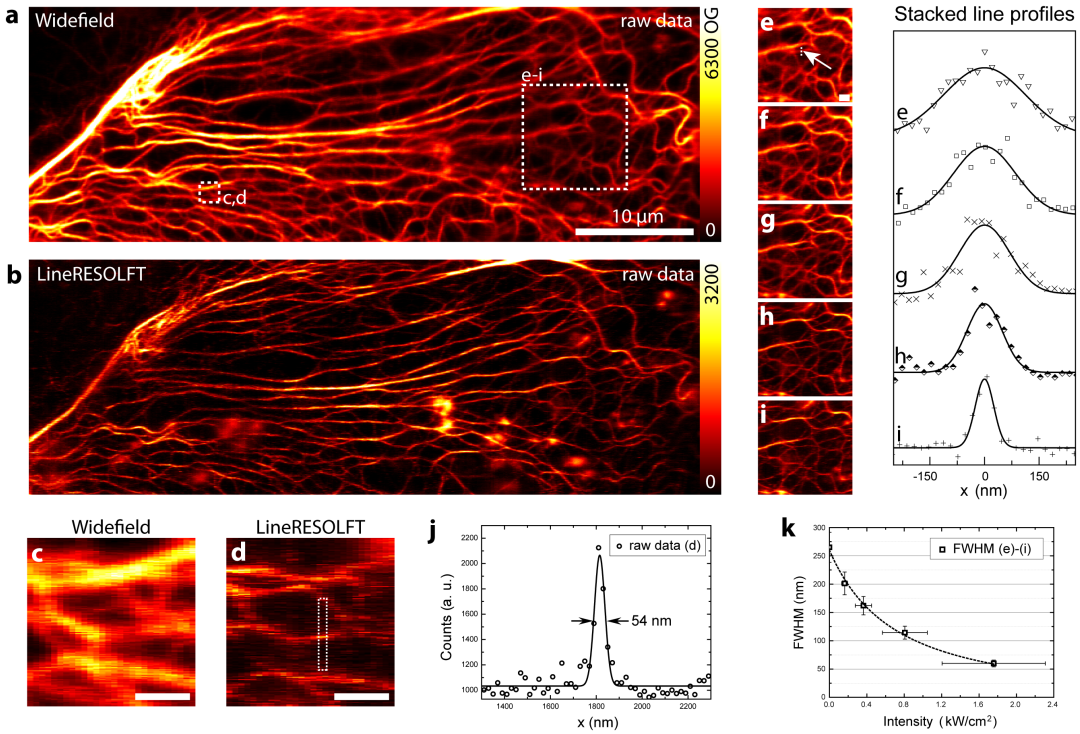

Figure 3.3: Resolution enhancement along the scanning direction - A living mammalian (PtK2) cell expressing keratin-19−rsEGFP imaged in widefield (**a**) and scanned vertically in the lineRESOLFT mode (**b**). The total image acquisition time was 30 s for a field of view of 57 µm x 20 µm. (**c**,**d**) A magnified view demonstrating the improved resolution. The two-pixel averaged line profile of **d** is shown in **j**. (**e-i**) Separate views of the indicated area when increasing the intensity of the deactivation beam (I_D). The corresponding line profiles of a thin filament (denoted by arrow) point out the narrowing of the microscope's PSF. The dependence of its FWHM on I_D is plotted in **k**. Scale bars: 1 µm, OG: overglow

To determine the required deactivation intensity I_D for a significant resolution enhancement, the power of the deactivation beam was varied and consecutive images were recorded. With a constant irradiation time of 10 ms, increasing I_D led to an improved resolution (Fig. 3.3e-i). Intensities of a few kW/cm^2 were sufficient to reach a resolution below 60 nm. The dependency of the resolution on I_D is depicted in Fig. 3.3k. With increasing I_D, the width of the effective PSF asymptotically approaches zero, following the relation FWHM $\rightarrow 1/\sqrt{I_D}$. Not surprisingly, an identical asymptotic behavior is found in STED microscopy[65], where similar switching kinetics apply, although on faster time scales. While all novel nanoscopy concepts promise unlimited resolution enhancement in theory, the attainable resolution is restricted experimentally. Practical limitations include, among others, non-ideal switching kinetics of the fluorophores, an unwanted residual intensity at the central "zero" of the deactivation PSF reducing signal to noise, and photobleaching. A special type of photobleaching displayed by rsFPs is the so called switching fatigue, addressing the inability to activate molecules beyond a certain amount of cycles. For lineRESOLFT with its highly efficient use of the switching cycles this is just a minor issue. In fact, after repeated imaging of identical FOVs, no photodamage was observed and photobleaching was very low (Fig. 3.3e-i). The possibility to verify and optimize the quality of the zero of the deactivation (see Chapter 2), a conceptual strength of the lineRESOLFT setup, guarantees a minimal residual deactivation intensity. Thus, the maximum photon count when applying the deactivation got reduced to just 50%, mainly attributed to the reduced spatial extent of the effective excitation PSF.

Reaching optimal imaging performance is not just a matter of the microscope and its conception, the properties of the fluorophores are equally important. Non-optimal switching kinetics, like cross-talk between activation and deactivation, may introduce a non-switchable background contribution. This leads to a broadening of the effective PSF impairing resolution improvement. Another critical point is the emitted photons per switching cycle. With more photons a higher signal-to-noise is reached, facilitating the discrimination of thin and dark filaments. To exclude limiting effects originating from the fluorophores and to exemplify the full capacity of the lineRESOLFT microscope, several reversible switchable proteins were tested. Additionally, multiple structures and cell types were targeted. Table 3.1 displays the variants used. Numerous

different combinations were imaged and subdiffraction resolution accomplished for all tested combinations. This confirms the versatility of the method.

Table 3.1: Versatility of lineRESOLFT imaging

Subdiffraction resolution achieved for:	
rsFPs	rsEGFP, rsEGFP(N205S), Dronpa-M159T
Targets	keratin-19, lifeact, homer, cytosol
Cells	PtK2, HeLa, neurons

For best imaging performance a bright signal is desirable. The number of emitted photons per switching cycle is limited, mainly due to the simultaneous deactivation during excitation. Thus, using slowly deactivating rsFPs which remain activated for longer periods, will increase signal-to-noise. rsEGFP(N205S), switching 3-fold slower compared to rsEGFP, therefore provides higher signal levels[43]. It facilitates higher resolution by enabling imaging of thin, dark filaments. This is illustrated in Fig. 3.4, which shows imaging of keratin filaments in a living HeLa cell.

First, only the two line-shaped illumination (activation and excitation) patterns were scanned vertically (Fig. 3.4a) to resemble a semi-confocal microscope. A second scan in lineRESOLFT mode, featuring the additional double-line-shaped deactivation pattern, resulted in superior resolution (Fig. 3.4b), revealing much more structural details. Since a cell is a three-dimensional object, suppressing out-of-focus background results in a better image quality. Thus, imaging the axially dense keratin network, covering most of the cell, profits from axial sectioning. Differential detection (DD) provides this improved axial discrimination, leading to better contrast. A comparison between semi-confocal and lineRESOLFT imaging (Fig. 3.4c,d) demonstrates the excellent resolving capability of the latter.

Comparing the resolutions reached for all tested rsFPs, it can be concluded that an rsFP facilitating imaging with a higher signal-to-noise allows higher resolution. In RESOLFT microscopy deactivation confines fluorescing molecules to an area much smaller than a diffraction-limited spot. The size of that area determines the achievable resolution. While increasing the deactivation intensity reduces the area of activated molecules and thus increases resolution, less molecules contribute to the fluorescence signal. However, experimentally a certain minimum signal level is required in order to be distinguishable from noise. Thus, depending on the brightness of the molecules,

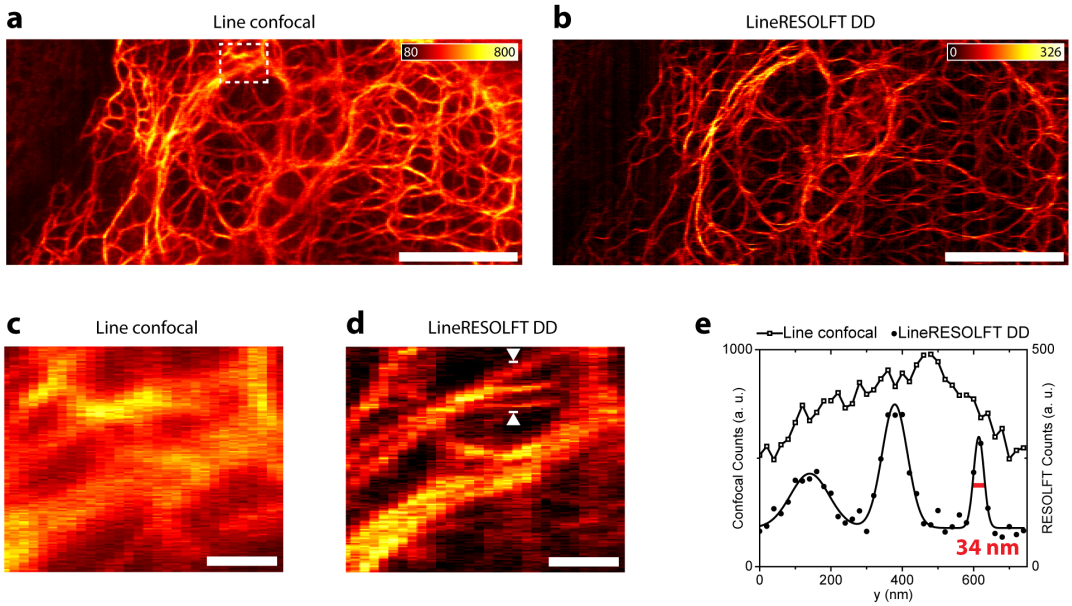

Figure 3.4: LineRESOLFT imaging with a more than 4-fold resolution enhancement - A living mammalian (HeLa) cell expressing keratin-19−rsEGFP(N205S) scanned vertically in the lineRESOLFT microscope without (**a**) and with (**b**) the deactivation pattern. Differential detection (DD) enhances contrast for areas with axially dense structures. (**c**,**d**) The magnified views of the indicated region demonstrate a superior resolution improvement. (**e**) The 2-pixel wide average line profile along the arrows proves a more than 4-fold resolution enhancement of the lineRESOLFT microscope compared to the diffraction limited (confocal) counterpart. While the RESOLFT image displays peaks fitted to Gaussians with individual FWHM of 127 nm, 83 nm and 34 nm, for the confocal case an identification of single peaks is impossible. Scale bars: 10 µm (**a**,**b**) and 1 µm (**c**,**d**)

decreasing the area of fluorescing molecules beyond a certain threshold will not result in a higher resolution but a loss of signal. Compared to an rsFP with faster switching, rsEGFP(205S) requires less activated molecules to maintain a sufficient signal level, enabling imaging with higher resolution. In addition it makes imaging more robust towards a suboptimal quality of the zero (caused by aberrations, switching cross-talk, etc.).

Precise assessment of the resolving power is complicated since in an image the width of the structure depends on both the structure size of the object (the sample), as well as on the effective PSF of the microscope. Measuring the imaged FWHM of thin filaments is an established estimate for resolution. Since for the figures presented in this section resolution improvement was only targeted along the vertical direction, horizontal filaments are used to assess resolving power.

In Fig. 3.4c,d three horizontal filaments are clearly separated under RESOLFT imaging while undistinguishable in the confocal case. A line profile along the indicated arrows was taken (Fig. 3.4e). To avoid artifacts a two pixel wide mean was applied, minimizing the contribution of noise. The fit to three Gaussian peaks results in individual FWHM down to 34 nm. According to the Nyquist-Shannon sampling theorem[51], a signal containing no higher frequency than f, is completely determined by sampling at points spaced $(2f)^{-1}$. For the presented images a scan step size of 20 nm was chosen. Thus the lineRESOLFT microscope enabled a resolution enhancement down to 40 nm, corresponding to a more than 4.5-fold gain over the Abbe limit ($\approx$ 185 nm, see Eq. 2.1).

To test the reproducibility of the results, several living cells were imaged. A selection is displayed in Fig. 3.5. LineRESOLFT imaging was performed by scanning the effective line PSF along the vertical direction, yielding a field of view of 42 x 19 µm^2 which is partly displayed. No post-processing, for example subtraction of out of focus signal or deconvolution, of the presented raw data was performed. Every image stems from a different cell.

Thin filaments could be identified regularly (Fig. 3.5a-c). Artifacts caused by disruptive movements of the piezo-scanner can be excluded. This would also be visible along the whole line and not just for the extent of the thin filament. Two pixel-wide average line profiles allow for a quantification of the resolving power (Fig. 3.5d-f). Gaussian fits reveal structure width around 40 nm. This confirms the excellent subdiffraction resolution of the lineRESOLFT microscope. The raw data images additionally prove

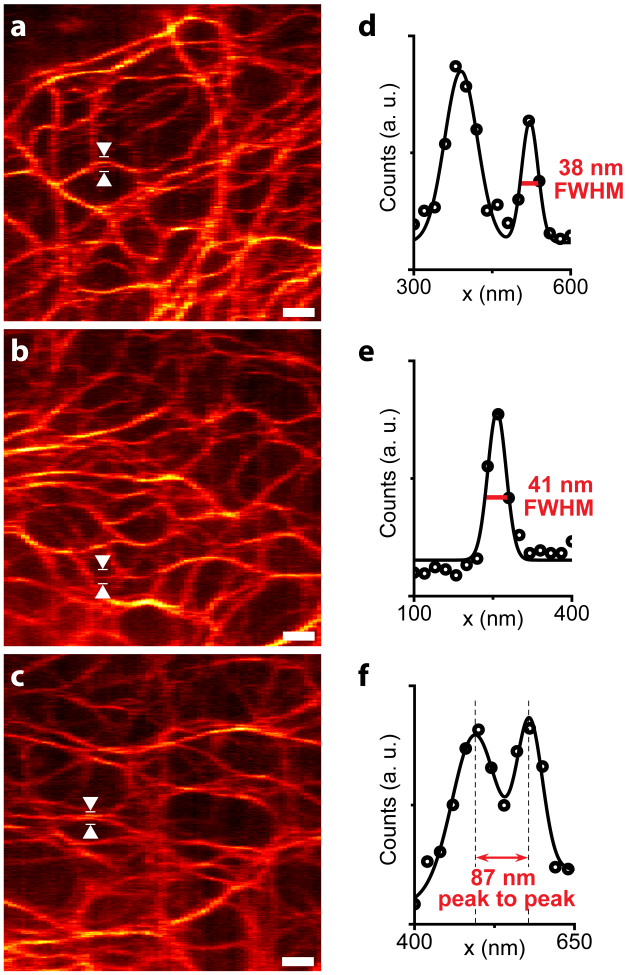

Figure 3.5: Examples of subdiffraction lineRESOLFT imaging - (**a-c**) Three different HeLa cells expressing keratin-19−rsEGFP(N205S) imaged with lineRESOLFT. Raw data of a vertical scan without differential detection is shown. (**d-e**) 2-pixel wide average line profile along the indicated arrows fitted to Gaussian. A reproducible resolution down to 40 nm is demonstrated. The peaks in (**f**) feature individual FWHM of 82 nm and 47 nm. Scale bars: 1 µm

that the differential detection as well as deconvolution are not necessary to reach high resolution.

A robust measure of performance is the ability to discriminate close filaments. Fig. 3.5c,f shows an image where two filaments in close proximity can be separated. With the individual widths of the filaments being 82 nm and 47 nm, a peak to peak distance of 87 nm is resolved, well beyond Abbe's diffraction limit.

In conclusion, here we demonstrated parallelized subdiffraction imaging along one direction with lineRESOLFT. Living cells were repeatedly imaged with a reproducible resolution of ∼40 nm. With point scanning RESOLFT typically reaching 35 - 50 nm resolution[38–40], this proves that the focal-plane resolution is neither theoretically, nor experimentally impaired by our parallelization scheme. The presented method was applied to a variety of different proteins, structures and cells. The versatility allows tuning the expression to meet specific biological problems, e. g. targeting for highest resolution or fastest image acquisition. Structural details close to each other and orthogonal to the line-shaped illumination were resolved. The following section will show how the excellent resolution improvement along the scanning direction is used to retrieve an image with spatially quasi-uniform subdiffraction resolution.

3.2.2 Rotation enables spatially quasi-isotropic resolution enhancement

The acquisition of several one-directional lineRESOLFT scans with varying scanning directions allows the combination into a final image which exhibits spatially quasi-uniform resolution. As explained in Section 2.1, each individual scan provides extended subdiffractional information along the scanning direction. A post-processing step including the mutual alignment (superimposition) and subsequent combined deconvolution is necessary. In this section the realization of this post-processing is discussed. First, the experimental accuracy of the superimposition will be assessed and second, we explain the combined deconvolution leading to an image of isotropic subdiffraction resolution.

Accuracy of the image superimposition

Of major practical relevance is the ability to superimpose subsequent lineRESOLFT scans acquired with varying oriented line-shaped illuminations. As an example, in order to target for a resolution of ∼50 nm, the superimposition accuracy should be below

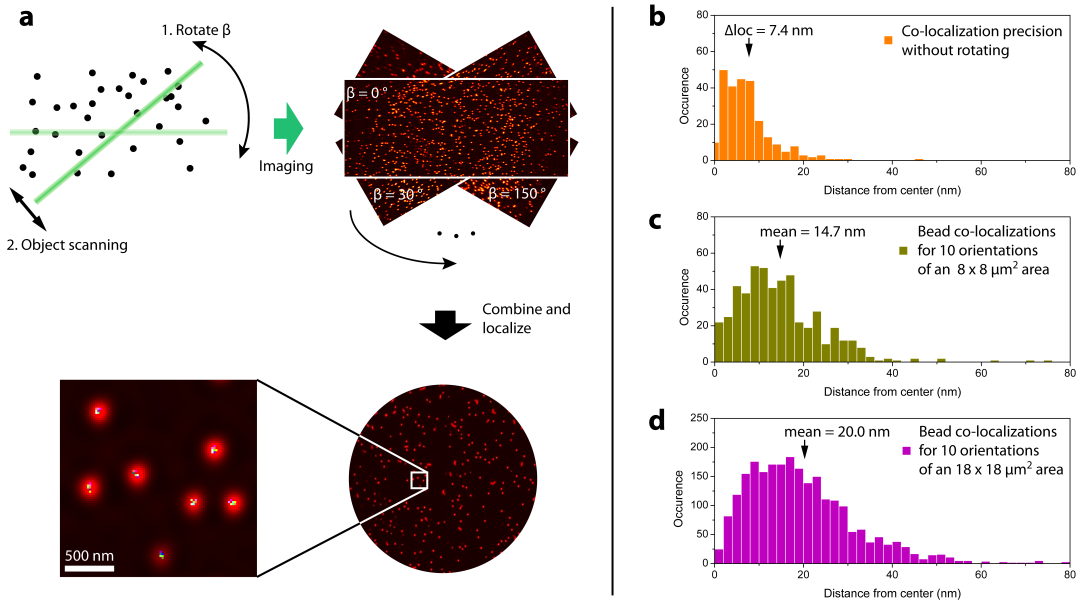

Figure 3.6: Co-localization precision of multiple orientations - (**a**) Schematic illustration of determining the co-localization: First, fluorescent nanobeads are consecutively imaged under varying orientations of the line-shaped illumination. Subsequent combination to a single image and localization of each bead position allows to investigate the accuracy of the rotation. (**b-d**) Statistics of the displacements of the apparent from the actual bead positions. While the displacements without rotation are mainly caused by Poisson noise (**b**), the (dis)ability to mutually align individual images within a target area additionally contributes to the error in co-localization when using multiple orientations (**c**,**d**)

this limit, preferably at least by a factor of two. For this task, home-built MATLAB routines were used to mutually align subsequent lineRESOLFT scans. An algorithm based on maximizing the cross-correlation determined an affine transformation for each individual scan, which accounts for rotation, shifting, scaling and shearing to optimize the overlap. These affine transformations co-align all subsequent scans with the first scan.

To test the accuracy of the setup and the algorithm, fluorescent nanobeads were imaged with ten different orientations of the line-shaped illumination (Fig. 3.6).

For each scan the algorithm calculated an affine transformation which provided best overlap with the first one. Subsequently, $N > 50$ beads, contained in all scans, were localized within a central area of 8x8 µm^2 or 18x18 µm^2. The localization precision only depends on the number of photons[66] (Fig. 3.6b). With rotation the apparent bead po-

sitions in the 10 scans additionally fluctuate around the actual (mean) position. The distribution of all $10N$ displacements characterizes the accuracy of the image registration (Fig. 3.6c,d). Resulting mean distances below 20 nm provide an upper boundary for the inaccuracy of the rotation. In reality, the rotation is more accurate because the bead localization works suboptimally for dim or non-spherical beads. Additionally, in rare cases it is difficult to determine the center of a bead if two beads happen to be close together (well below the diffraction limit). This inefficiencies when localizing beads produce outliners in the presented statistics. They are not caused by the algorithm used to optimize the affine transformations, which works via cross-correlation, but caused by the subsequent localization algorithm. Since the localization algorithm was only used for testing purposes, we conclude that in principle the rotation scheme allows an image registration of an accuracy better than 20 nm. The accuracy of the actual calculated co-alignment depends on the performance the implemented algorithm. Unfortunately, a direct assessment of the accuracy of the cross-correlation algorithm when measuring cells is not possible. However, individual inspection of co-aligned scans of cells suggest an accuracy comparable to the presented bead-based tests.

Combined deconvolution retrieves isotropic resolution

Once the affine transformations to superimpose individual, one-directionally scanned images are determined, a subsequent combined deconvolution step is necessary. In this step the structural details of the multiple scans of the same object but with different scanning directions get combined to render one final image exhibiting the highest information content.

Here we used an iterative, nonlinear image deconvolution algorithm based on Richardson[67] and Lucy[68]. A maximum likelihood estimation using different (rotated) effective PSFs for each available image can reconstructs an object that best represents all recorded scans[69,70]. In short, the method averages all update factors resulting from single images using their specific PSFs on a common estimate of the object. Applying the averaged update factor provides the estimate used for the next iteration. The process was stopped after 40 iterations. The algorithm has the advantage of constraining the object to non-negative values, corresponding to the physical reality that the dye density is non-negative. Similar iterative nonlinear methods exist, having been "routinely used with success by biologists" [71].

Fig. 3.7 displays the resulting object (living HeLa cell expressing keratin-19−rsEGFP-(N205S)) deconvolved from four scans. For each subsequent scan the line-shaped illumination was rotated by 45°. To compare the results an identical procedure was applied to line confocal and lineRESOLFT imaging of the same field of view. A resolution enhancement for each individual lineRESOLFT scan was observed (not displayed here). The deconvolved final image clearly features an improved resolution along all directions (Fig. 3.7a). Thin keratin filaments and a substantially higher level of detail are visible − for example along vertical, horizontal as well as diagonal directions − whereas the confocal combined deconvolution is blurred. To exemplify the enhanced separation of filaments a magnified view is provided (Fig. 3.7b,c). To assure that the appearance of separated filaments is not an artifact of the superimposition and/or deconvolution, we identified identical distinct filaments in the raw data. It was confirmed that the deconvolution only combines structural information and resolution enhancement already present in the original (raw) data.

Noise within the raw data is a challenge for every deconvolution algorithm. A deconvolution could mistake noisy pixel values for real structures. In the deconvolved RESOLFT image this behaviour can be partly observed. A priori knowledge like a constraint to connected filaments, corresponding to an absence of point-like objects, would improve contrast further[72]. However, in order to make the deconvolution more robust, no such extra assumptions were used.

Evaluating the resolution of an optical system is relative straightforward for raw data, where FWHM of the blurred objects are determined. For deconvolved data no such simple criterion exists. A point-like object restored from a blurred image can be confined to a substantially smaller volume[73,74]. Thus, a more general measure for resolution is the capability to "sufficiently" distinguish details. The precise definition of what constitutes "sufficiently" varies[75]. The Sparrow criterion defines two objects as just resolved when the dip between them just disappears, while the well-known Rayleigh criterion requires the dip to be at least $\approx 26\%$ in contrast[76]. This theoretical simple task is experimentally demanding, because the ability to find thin and bright structures in close proximity strongly depends on the sample.

Figure 3.7d quantifies the distance between two filaments which are resolved. A 10-pixel-wide average line profile is fitted to a sum of two Gaussians with individual FWHM of 100 nm and 87 nm. The peaks with a separation of 84 nm can be distinguished.

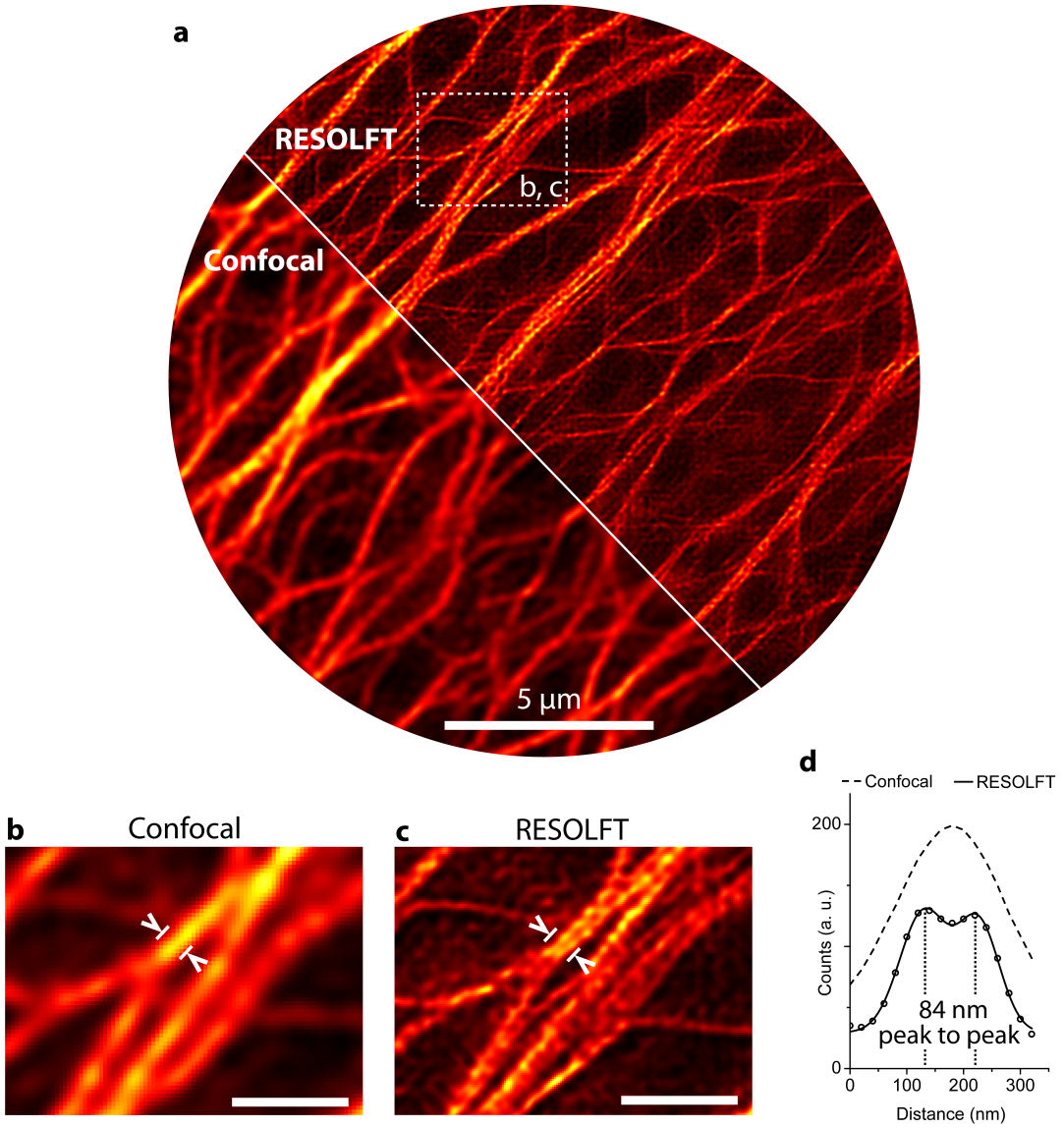

Figure 3.7: Deconvolved images with quasi-isotropic resolution - (**a**) A deconvolution of four scans with different orientations of the line-shaped illumination. RESOLFT imaging provides a strong resolution enhancement in any direction. (**b**,**c**) Magnified views of the indicated area. A direct comparison reveals much more structural information for the RESOLFT mode. (**d**) A 10-pixel-average line profile demonstrates that close filaments which remain unresolved in confocal mode, get separated when imaging in RESOLFT mode. The fit to a sum of two Gaussians results in a peak to peak distance of ∼84 nm. Pixel size: 20 x 20 nm^2, Scale bars: 5 µm (top), 1 µm (bottom)

In summary, this section illustrated how the superior subdiffraction resolution of single lineRESOLFT scans get extended to all directions when rotating the line pattern. The approach renders quasi-isotropic resolution in the focal plane. While more directions will lead to a more homogeneously uniform resolution, practical considerations suggest a trade-off between imaging speed, usability and the level of isotropy. Here we demonstrated that four rotations lead to a resolution well beyond the diffraction barrier along all lateral directions, experimentally confirming previously theoretical considerations (see Section 2.1).

Chapter 4

Biological application

4.1 Dynamics in living brain slices

Dendritic spines, the tiny outgrowths on the dendrites of neurons, play a key role in brain activity. They form synapses with axons of other neurons thereby establishing the inter-connectivity of neurons. They are regarded to be central to learning and memory. Therefore precise determination of their morphology and temporal variation are essential to understand brain function. Imaging the amount, shape and motility of spines gives valuable insight to the neurosciences[77]. This requires novel nanoscopy methods to non-invasively resolve the fine details of synapses[30].

While neuronal activity is best studied *in vivo*, experimental realization is very demanding[31] (need to anesthetize, breathing introduces vibrations, etc.). Imaging organotypical brain slices simplifies the experiment while preserving the natural interconnectivity, function and environment of neurons. The advantage of a minimal disruption of tissue for brain slices is evident when put into contrast with the preparation of neurons in culture where initially, all natural interconnections between single neurons are lost, with only a partial regrowth after some time. Individual neurons only retain their functionality, but the neuronal network is lost.

Insights to brain functions requires studies of its dynamics. Researching the processing of signals by monitoring organization and interconnection of neurons requires the combination of non-invasive high resolution power with fast and low irradiation image acquisition. Here we will show that the lineRESOLFT microscope is an outstanding tool to tackle this challenging task.

The dynamics of dendritic spines in a living hippocampal brain slice of newborn mice is illustrated in Fig. 4.1. The widefield image visualizes Lifeact labelled F-actin inside spines along a dendrite. An undesirable high background caused by excitation of out of focus structures demonstrates an inherent disadvantage when imagining in widefield mode (Fig. 4.1a). Because of the three-dimensional extent of the dendrites, and cells in tissue in general, axial sectioning is required to discriminate between spines. The axial sectioning lineRESOLFT imaging combined with the differential detection enables mapping the morphology of individual dendritic spines and filopodia (Fig. 4.1b,c). To represent a 2D image of a three-dimensional organization, a maximum intensity projection over 5 µm in z is displayed. Color-coding the axial sections (see inlets) demonstrates the quasi-confocality of the method, highlighting the non-planar orientation of spines. To exemplify individual spine motility, magnified views are provided (Fig. 4.1*i*,*ii*). Projections over three planes were sufficient, because they already contained the spines completely. Line profiles were extracted from non-projected raw data, clearly showing resolution well beyond the diffraction limit (Fig. 4.1*iii*-*v*). The high resolution allows a detailed visualization of close structural features. The thinnest structures with $FWHM \approx 70\,\text{nm}$ indicate that the resolving power is at least of that order. Increasing the deactivation intensity between (Fig. 4.1b) and (Fig. 4.1c) did not result in the observation of thinner structures. The spine necks can therefore be assumed to be at least that large, which is in accordance with a typical variation in spine neck diameter of 40 nm to 500 nm in CA1 pyramidal neurons[78]. Subdiffraction resolution additionally allowed the observation of distinct ring-like actin substructures[47,79] on some of the spines (e. g. Fig. 4.1b,c, left edge).

The high dynamic range of the images is note-worthy: The ability to register low to very high photon signals within a single scan, facilitates imaging of thin and dark spines next to bright structures without saturating the detector.

To stimulate spontaneous neuronal activity, short-term treatment with an artificial cerebrospinal fluid containing elevated K^+ and reduced Na^+ levels was performed. This high-K^+ stimulation globally activates hippocampal neurons by depolarizing the membrane potential and holding it close to 0 mV. This greatly increases the spontaneous activation of synapses throughout the entire brain slice and has been shown to induce growth of new filopodia and dendritic spines, induce morphological changes of

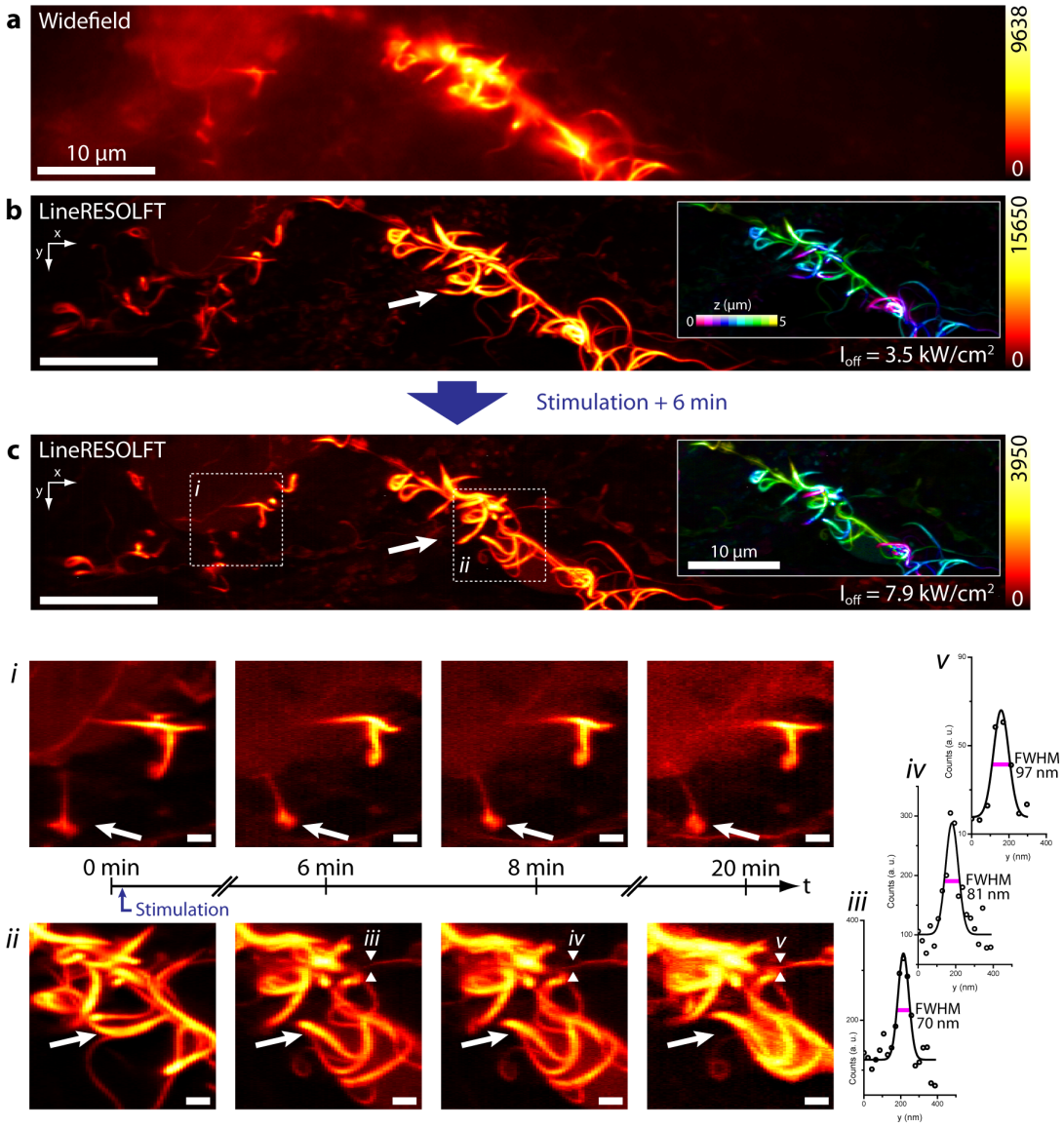

Figure 4.1: Stimulation of neurons in a living brain slice - A brain slice expressing Lifeact−Dronpa-M159T fusion protein imaged in widefield (**a**) and scanned along y in lineRESOLFT mode (**b**, **c**) for multiple z planes, before (**a**, **b**) and after (**c**) stimulation. In (**b**, **c**) the axial maximum intensity projection of the recorded xyz-stack of 87 µm x 19 µm x 5 µm (640 px x 950 px x 10 px) is shown. Total image acquisition time: 1.9 s (xy), 30 s (xyz). The inlets show an axial color-coding of the central volume. (***i***, ***ii***) Magnified views of the indicated regions under continuous lineRESOLFT imaging exemplify dendritic spine dynamics pre- and post-stimulation. The projection of three planes, 0.5 µm apart in z, is shown. The arrows denote moving structures. (***iii-v***) Line profiles of a single z-section fitted with Gaussians. All images display raw data of differential detection using normalized, nonlinear intensity scales to highlight thin filaments over bright, thick fibers ($SNR > 100$). Scale bars: 10 µm (**a-c**) and 1 µm (***i***,***ii***).

existing spines and increase other activities, such as microtubule invasion of dendritic spines[80,81]. The frequency and duration of the stimulation (repetitive over stationary) help determine whether or not the observed changes are merely transient or lasting in nature.

Imaging identical fields of view pre- and post-treatment revealed movement of spines and filopodia (see Fig. 4.1b,c), which substantiates their participation in signal processing. With the low photobleaching of the lineRESOLFT method, long-term dynamics could be monitored. Repetitive imaging, totalling 180 z-stacks, each recorded in 1.9 s, illustrates spine motion for up to 30 minutes. No damage of the dendrite nor individual spines was observed.

To investigate spine activity further, focussing more on short-term changes, we continuously imaged another area of the hippocampal CA1 region under lineRESOLFT illumination for a single z-plane (see Fig. 4.2). An image acquisition time below 2 s per frame facilitated the detection of rapid spine motility on the second time scale. Recording 50 images in under 100 s without any visible damage emphasizes the low phototoxicity of the method. RESOLFT features ultra-low intensities as well as a low total light-dose. Line scanning additionally does not require a high amount of switching cycles per frame which allowed continuous recording of a large area without needing to wait for a replenishment of the fluorophores. Not surprisingly, the thin, less bright spines show the highest motility. Since the lifeact label attaches to actin, reduced brightness indicate a low incorporation of stabilizing actin filaments, making the spines more flexible. While most of the thick and bright spines remain almost unchanged, a rapid shifting of thin spines is observed. In the magnified view (Fig. 4.2*i*) the fast dynamics of two spines in close proximity in the second time scale is resolved. Initially, one of the dendritic spines, with a neck diameter of less than 120 nm, is covered by another one. It becomes visible when they are shifting apart. Subdiffraction resolution is essential to discriminate between the individual spines. Subsequently, the head gets pulled back, closer to the dendrite. Spine activity was observed in several areas, see Fig. 4.2*ii*. This highlights the novel opportunity to monitor fast dynamics of spines activity with high-resolution for large fields of view.

A comparison between nanoscopy methods, which have been applied to imaging spines in living brain slices or *in vivo*, clearly shows the vast increase in imaging speed.

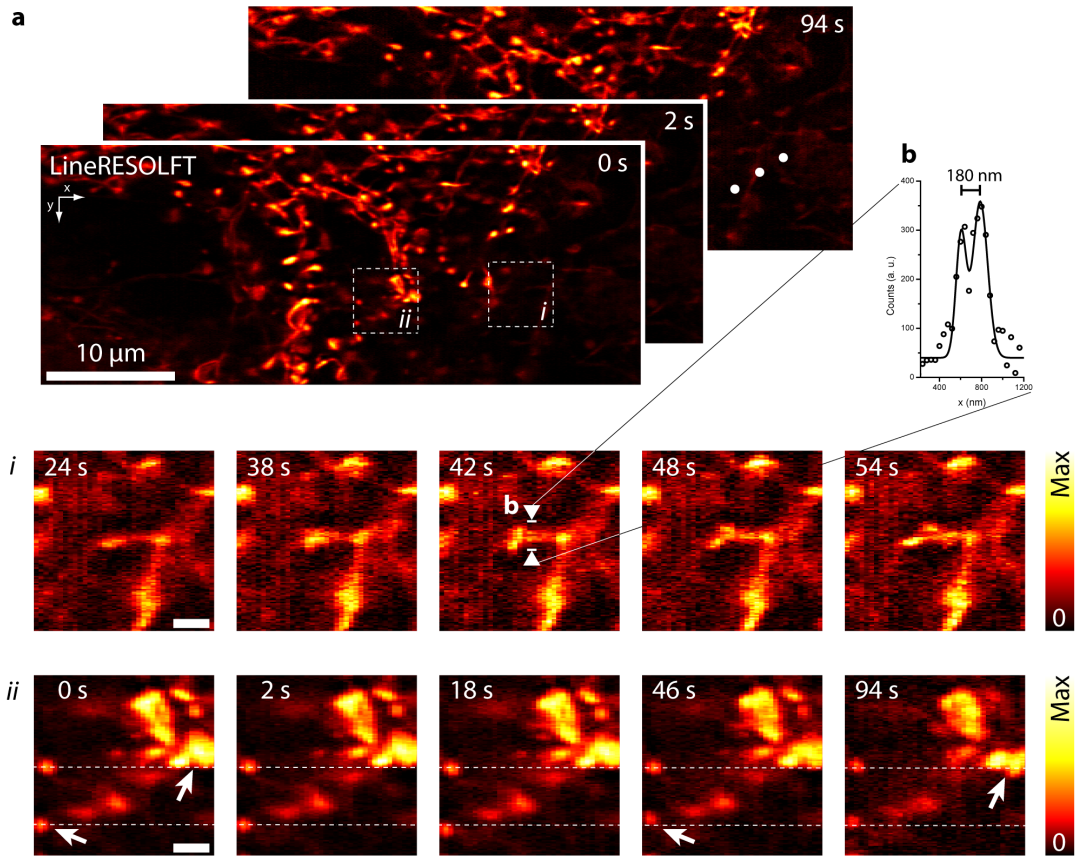

Figure 4.2: Fast dynamics of dendritic spines in a living brain slice - (**a**) Continuous lineRESOLFT imaging of a living brain slice expressing Lifeact−Dronpa-M159T fusion. A central part of the total field of view of 87 µm x 19 µm (640 px x 950 px) is displayed. Total image acquisition time: 1.9 s per frame. (***i***, ***ii***) Magnified views of the indicated regions in (**a**). Rapid spine motility on the second time scale can be observed. In (***i***) high spatio-temporal resolution of the independent movement of two individual spines is shown. Initially being in front of each other, they quickly shift apart. (**b**) Two pixel average line profile of raw data, fitted to a sum of two Gaussians with individual *FWHM* of 115 nm and 166 nm. The arrows in (***ii***) highlight rapidly shifting structures. All images display raw data of differential detection using normalized, linear (***i***) or nonlinear (**a**, ***ii***) intensity scales to best highlight thin filaments over bright, thick fibers. Scale bars: 10 µm (**a**) and 1 µm (***i***,***ii***).

Previously reported acquisition times for subdiffraction imaging of spines for a field of view of 20 x 20 µm^2 ranged from >10 s using STED[31,82] to >1 min using the low light-dose RESOLFT[47]. PALM measurements imaged spine dynamics at time intervals >25 s in fixed neurons[79]. The parallelization in lineRESOLFT allows to reduce the imaging time to 2 s. In fact the acquisition time is independent of the length in x, readily demonstrated by the extension of the FOV to 87 x 20 µm^2. Recording an equally sized image with point scanning RESOLFT would take at least 4 min. In the presented experiments resolution enhancement was targeted only for the y-direction. For isotropic super-resolution, the acquisition of $m > 6$ rotated images is necessary (see Ch. 2), leading to an imaging speed comparable to STED. Because of the linear, instead of quadratic scaling of the acquisition time with the imaged area, increasing the field of view would quickly regain the lineRESOLFT advantage (concerning the acquisition time).

To summarize the experiments, first we demonstrated the excellent optical sectioning of lineRESOLFT enabling the subdiffraction imaging of thick tissue. However, in this thesis, all measurements were performed close to the surface with penetration depths of just a couple of micrometers. As for most optical microscopy techniques, tissue penetration is limited due to scattering and aberrations. Spherical aberrations caused by the refractive index mismatch of the oil-immersion to the brain tissue[83] contribute the most. The use of glycerol-immersion objectives allow a correction of spherical aberrations which can extend penetrations depth of nanoscopy methods to up to 120 µm, as was reported before[82]. As it should be straightforward to apply the same approach to the lineRESOLFT microscope, we are planning to follow up with imaging deep inside tissue.

Further, high-resolution well beyond the diffraction limit of conventional microscopy enabled imaging of fine neuronal details and discrimination of substructures within dendritic spines. Continuous imaging highlighted the short- and long-term dynamics of dendritic spines for spontaneous activation of synapses. With a 100-fold faster image acquisition compared to point scanning RESOLFT, movements of spines within a few seconds were visualized.

Whereas nanoscopy of rapid spine motility on the second time scale was previously only achieved by a strong reduction of the field of view[31,47,82], we were able to track

fast dynamics within a large area of roughly 80 x 20 µm^2. LineRESOLFT imaging enabled simultaneous investigation of spines separated by tens of micrometers. A reduced number of switching cycles allowed imaging of a slow-replenishing actin label, which provides more structural insight than e. g. a voluminous cytosol label. Measuring with low light intensities as well as a low total light dose results in low photobleaching which, besides facilitating long-term imaging, minimizes the risk of introducing phototoxic stress. This novel method to research the nanoscopic dynamics of distant spines with high resolution gives rise to exciting opportunities to extend our knowledge of brain function.

Chapter 5

Conclusions and outlook

In this thesis, lineRESOLFT was presented, a method for the parallelization of scanning-based, diffraction-unlimited, optical sectioning RESOLFT. The experimental realization enabled non-invasive three-dimensional imaging of large fields of view of living tissue with high spatio-temporal resolution at low light levels.

Parallelization of RESOLFT nanoscopy

Opting for a line implementation, it was made possible to parallelize RESOLFT and substantially speed up imaging. Line-shaped intensity minima, formed by a cylindrical lens and a phase plate, were used for the deactivation. The length of the line can be varied by using cylindrical lenses of different focal lengths and thus be adapted to the experimental needs. We achieved a line length of ∼70 µm (FWHM), a 350-fold parallelization over a diffraction limited spot (∼0.2 µm). This high degree of parallelization was produced without impairing resolution.

Live-cell lineRESOLFT imaging of large fields of view reached a lateral resolution of ∼40 nm, similar to point scanning RESOLFT, typically reaching 35 - 50 nm resolution[38–40]. While recently reported widefield-based parallelization schemes covered larger fields of view, they either could just reach 80 nm resolution[43] or were still slow[42]. As reported here, lineRESOLFT provides both high spatial and temporal resolution for large fields of view, as it was successfully demonstrated by the investigation of spine dynamics on the second time scale. The monitoring of rapid spine motility was accompanied by the discrimination of fine structural details, unresolvable to confocal microscopy. Nevertheless, when comparing the imaging times to other schemes,

it should be taken into account that the high-speed lineRESOLFT images targeted a diffraction-unlimited resolution along just one direction. Subdiffraction resolution along one direction is sufficient for specific biological applications, where certain a priori knowledge about the object is available. For example, in the case of round vesicles, a single scan would provide their diameter and the position of their center and thus contain all necessary information to reconstruct the object. Another example where a single 1d scan is sufficient are co-linear line-shaped structures like parallel filaments. The required pattern rotation for isotropic lineRESOLFT adds complexity and the need for deconvolution. However, we demonstrated the possibility of achieving quasi-isotropic subdiffraction resolution by co-aligning multiple scans and by using a combined deconvolution.

The speed sensitive part of our setup was the mechanical rotation ($\sim$5 s per orientation). While state of the art rotation stages could speed up the rotation 10-fold, the vulnerability to mechanical drift would remain. Developing a scheme, which could reconstruct the image from scanning under continuous rotation, abandoning the need to repeatedly accelerate, would render the imaging process substantially faster and more stable. Another approach, an implementation based on a spatial light modulator (SLM), seems equally promising. Structured illumination microscopy, facing similar challenges, has benefited from this approach, where an SLM-based pattern rotation enabled video-rate image acquisition[16].

Clearly, lineRESOLFT does not target on competing with widefield-based parallelization schemes for speed. Instead, lineRESOLFT complements these widefield-based techniques, by offering strong optical section.

Non-invasive optical sectioning

While confocal microscopes exhibit strong optical sectioning, widefield illumination induces a high out-of-focus background, potentially obscuring in-focus details. Thus, the infinite plane response (IRF), representing the fluorescence contribution of a fluorescent sheet located at a distance z away from the focal plane, while being constant for the widefield microscope, decays with z^{-2} (for $z > 2\,\mu\text{m}$) in the confocal case. In Chapter 2 we demonstrated, that optical sectioning is fundamentally inherent to line microscopes, for which the IRF decays with z^{-1}. Furthermore, we introduced a detection scheme for high NA objectives, previously reported only for low NA, that increases the sectioning

further, beyond that of the confocal microscope. The implementation of a differential detection (DD) results in an IRF-decay with $z^{-2.9}$. The theoretical derivations were experimentally confirmed by measuring the response of a thin fluorescent membrane when defocussing.

Since at least two detectors are used for DD, each contributing with individual noise, the increased contrast comes at the cost of (slightly) lower signal-to-noise levels, depending on the number of detectors averaged over. Thus, for dim samples, it might be preferable not to use DD. Since in our lineRESOLFT implementation all camera data was stored without discarding any lines, the application of DD can be readily reversed, meeting the experimental needs.

Illustrating the power of lineRESOLFT DD, the presented data on three-dimensional lineRESOLFT imaging of living cells exhibited strong reduction of out-of-focus background when using DD. A pronounced increase in contrast was visible for axially dense structures.

Studying dynamics on the second time scale

The confocality of lineRESOLFT facilitated imaging of thick tissue with diffraction-unlimited lateral resolution. Due to the low light intensities employed, photobleaching and photodamage were minimized. Demonstrating the full potential of the method, continuous lineRESOLFT imaging of large fields of view enabled the observation of the dynamics of distant spines with subdiffraction resolution and on the second time scale. For the first time, fast three-dimensional RESOLFT imaging of living tissue with subdiffraction resolution and a high degree of parallelization was achieved.

Aberrations caused by an refractive index mismatch between the oil objective and the sample prevented from imaging at penetration depths deeper than $\sim$5 µm. As has been demonstrated before, these spherical aberrations can be corrected with appropriate optics[47,82,84,85]. Incorporating these corrections to the lineRESOLFT setup should be straightforward[47,82] and would allow penetration depth of $\sim$50 µm.

Outlook

Continuing progress in camera technology is likely to increase frame rates even further. A negligible time for reading out the camera combined with low read noise, would enable measuring the switching kinetics during imaging. Instead of exposing the camera for

a time t, the fluorescence signal could be recorded at multiple (n) time intervals t/n, without reducing imaging speed. Thus, when illuminating negative switching rsFPs, which get excited and switched off at the same wavelength, the time-dependent signal decay could be extracted, opening new opportunities. For example, by recording the fluorescence for the deactivation as well as for the excitation, a potential cross-talk could be corrected for. As studies of related processes suggest [86,87], this would result in a better contrast and higher resolution. Additionally, with high-speed low-noise cameras and a further development in fast switching rsFPs, lineRESOLFT has the potential to resolve many biological processes in real-time.

Future advances, focussing on the switching processes of rsFPs, might lead to an even higher increase in sectioning and penetration depth. With switching induced by a two-photon process, RESOLFT could reach much deeper penetration depths, as does two-photon microscopy [58]. Since two-photon switching would require substantially higher light intensities, available laser sources would not permit simultaneous coverage of very large areas. Thus, two-photon lineRESOLFT would be the natural method of choice for parallelization.

References

[1] Abbe, E. **Beiträge zur Theorie des Mikroskops und der mikroskopischen Wahrnehmung**. *Archiv f. mikrosk. Anatomie*, **9**(1):413–468, December 1873. [cited on pp. 1, 9, 13]

[2] Hell, S. **Double-confocal scanning microscope**, June 1992. EU Patent No. 0491289 (A1). [cited on pp. 1, 27]

[3] Hell, S. and Stelzer, E.H.K. **Properties of a 4Pi confocal fluorescence microscope**. *J. Opt. Soc. Am. A*, **9**(12):2159–2166, December 1992. [cited on p. 1]

[4] Gustafsson, M.G.L., Agard, D.A. and Sedat, J.W. **I5M: 3D widefield light microscopy with better than 100 nm axial resolution**. *J. Microsc.*, **195**(1):10–16, 1999. [cited on p. 1]

[5] Gugel, H., Bewersdorf, J., Jakobs, S., Engelhardt, J., Storz, R. and Hell, S.W. **Cooperative 4Pi Excitation and Detection Yields Sevenfold Sharper Optical Sections in Live-Cell Microscopy**. *Biophys. J.*, **87**(6):4146–4152, December 2004. [cited on p. 1]

[6] Kirz, J., Jacobsen, C. and Howells, M. **Soft X-ray microscopes and their biological applications**. *Q. Rev. Biophys.*, **28**(1):33–130, February 1995. [cited on p. 2]

[7] Shapiro, D. et al. **Biological imaging by soft x-ray diffraction microscopy**. *PNAS*, **102**(43):15343–15346, October 2005. [cited on p. 2]

[8] Erni, R., Rossell, M.D., Kisielowski, C. and Dahmen, U. **Atomic-Resolution Imaging with a Sub-50-pm Electron Probe**. *Phys. Rev. Lett.*, **102**(9):096101, March 2009. [cited on p. 2]

[9] Lewis, A., Taha, H., Strinkovski, A., Manevitch, A., Khatchatouriants, A., Dekhter, R. and Ammann, E. **Near-field optics: from subwavelength illumination to nanometric shadowing**. *Nat. Biotech.*, **21**(11):1378–1386, November 2003. [cited on p. 2]

REFERENCES

[10] Binnig, G., Quate, C.F. and Gerber, C. **Atomic Force Microscope**. *Phys. Rev. Lett.*, **56**(9):930–933, March 1986. [cited on p. 2]

[11] Coons, A.H., Creech, H.J., Jones, R.N. and Berliner, E. **The Demonstration of Pneumococcal Antigen in Tissues by the Use of Fluorescent Antibody**. *J. Immunol.*, **45**(3):159–170, November 1942. [cited on p. 3]

[12] **Seeing is believing**. *Nat. Methods*, **2**(12):889–889, December 2005. [cited on p. 3]

[13] Minsky, M. **Microscopy apparatus**, December 1961. US Patent No. 3013467 (A). [cited on p. 3]

[14] Müller, C.B. and Enderlein, J. **Image Scanning Microscopy**. *Phys. Rev. Lett.*, **104**(19):198101, May 2010. [cited on p. 3]

[15] Gustafsson, M.G.L. **Surpassing the lateral resolution limit by a factor of two using structured illumination microscopy**. *J. Microsc.*, **198**(2):82–87, 2000. [cited on p. 3]

[16] Kner, P., Chhun, B.B., Griffis, E.R., Winoto, L. and Gustafsson, M.G.L. **Super-resolution video microscopy of live cells by structured illumination**. *Nat. Methods*, **6**(5):339–342, May 2009. [cited on pp. 3, 56]

[17] Hell, S.W. **Toward fluorescence nanoscopy**. *Nat. Biotech.*, **21**(11):1347–1355, November 2003. [cited on pp. 3, 4, 9]

[18] Rust, M.J., Bates, M. and Zhuang, X. **Sub-diffraction-limit imaging by stochastic optical reconstruction microscopy (STORM)**. *Nat. Methods*, **3**(10):793–796, October 2006. [cited on p. 4]

[19] Betzig, E., Patterson, G.H., Sougrat, R., Lindwasser, O.W., Olenych, S., Bonifacino, J.S., Davidson, M.W., Lippincott-Schwartz, J. and Hess, H.F. **Imaging Intracellular Fluorescent Proteins at Nanometer Resolution**. *Science*, **313**(5793):1642–1645, September 2006. [cited on p. 4]

[20] Hess, S.T., Girirajan, T.P. and Mason, M.D. **Ultra-High Resolution Imaging by Fluorescence Photoactivation Localization Microscopy**. *Biophysical Journal*, **91**(11):4258–4272, December 2006. [cited on pp. 3, 4]

[21] Westphal, V., Rizzoli, S.O., Lauterbach, M.A., Kamin, D., Jahn, R. and Hell, S.W. **Video-Rate Far-Field Optical Nanoscopy Dissects Synaptic Vesicle Movement**. *Science*, **320**(5873):246–249, April 2008. [cited on pp. 3, 4]

[22] Hell, S.W. **Microscopy and its focal switch**. *Nat. Methods*, **6**(1):24–32, January 2009. [cited on pp. 3, 9]

[23] Hell, S.W. and Wichmann, J. **Breaking the diffraction resolution limit by stimulated emission: stimulated-emission-depletion fluorescence microscopy**. *Opt. Lett.*, **19**(11):780–782, June 1994. [cited on p. 4]

[24] Klar, T.A., Jakobs, S., Dyba, M., Egner, A. and Hell, S.W. **Fluorescence microscopy with diffraction resolution barrier broken by stimulated emission**. *PNAS*, **97**(15):8206–8210, July 2000. [cited on p. 4]

[25] Westphal, V. and Hell, S.W. **Nanoscale Resolution in the Focal Plane of an Optical Microscope**. *Phys. Rev. Lett.*, **94**(14):143903, April 2005. [cited on p. 4]

[26] Göttfert, F., Wurm, C.A., Mueller, V., Berning, S., Cordes, V.C., Honigmann, A. and Hell, S.W. **Coaligned Dual-Channel STED Nanoscopy and Molecular Diffusion Analysis at 20 nm Resolution**. *Biophys. J.*, **105**(1):L01–L03, July 2013. [cited on p. 4]

[27] Rittweger, E., Han, K.Y., Irvine, S.E., Eggeling, C. and Hell, S.W. **STED microscopy reveals crystal colour centres with nanometric resolution**. *Nat. Photonics*, **3**(3):144–147, March 2009. [cited on p. 4]

[28] Hein, B., Willig, K.I. and Hell, S.W. **Stimulated emission depletion (STED) nanoscopy of a fluorescent protein-labeled organelle inside a living cell**. *PNAS*, **105**(38):14271–14276, September 2008. [cited on p. 4]

[29] Eggeling, C. et al. **Direct observation of the nanoscale dynamics of membrane lipids in a living cell**. *Nature*, **457**(7233):1159–1162, February 2009. [cited on pp.]

[30] Nägerl, U.V., Willig, K.I., Hein, B., Hell, S.W. and Bonhoeffer, T. **Live-cell imaging of dendritic spines by STED microscopy**. *PNAS*, **105**(48):18982–18987, December 2008. [cited on p. 47]

[31] Berning, S., Willig, K.I., Steffens, H., Dibaj, P. and Hell, S.W. **Nanoscopy in a Living Mouse Brain**. *Science*, **335**(6068):551–551, February 2012. [cited on pp. 4, 47, 52]

[32] Huang, B., Babcock, H. and Zhuang, X. **Breaking the Diffraction Barrier: Super-Resolution Imaging of Cells**. *Cell*, **143**(7):1047–1058, December 2010. [cited on p. 4]

[33] Dertinger, T., Colyer, R., Iyer, G., Weiss, S. and Enderlein, J. **Fast, background-free, 3D super-resolution optical fluctuation imaging (SOFI)**. *PNAS*, **106**(52):22287–22292, December 2009. [cited on p. 4]

[34] Cox, S., Rosten, E., Monypenny, J., Jovanovic-Talisman, T., Burnette, D.T., Lippincott-Schwartz, J., Jones, G.E. and Heintzmann, R. **Bayesian localization**

microscopy reveals nanoscale podosome dynamics. *Nat. Methods*, **9**(2):195–200, February 2012. [cited on p. 4]

[35] Huang, F. et al. **Video-rate nanoscopy using sCMOS camera-specific single-molecule localization algorithms**. *Nat. Methods*, **10**(7):653–658, July 2013. [cited on p. 4]

[36] Tsien, R.Y. **The Green Fluorescent Protein**. *Annu. Rev. Biochem.*, **67**(1):509–544, 1998. [cited on p. 4]

[37] Hofmann, M., Eggeling, C., Jakobs, S. and Hell, S.W. **Breaking the diffraction barrier in fluorescence microscopy at low light intensities by using reversibly photoswitchable proteins**. *PNAS*, **102**(49):17565–17569, December 2005. [cited on p. 4]

[38] Grotjohann, T., Testa, I., Leutenegger, M., Bock, H., Urban, N.T., Lavoie-Cardinal, F., Willig, K.I., Eggeling, C., Jakobs, S. and Hell, S.W. **Diffraction-unlimited all-optical imaging and writing with a photochromic GFP**. *Nature*, **478**(7368):204–208, October 2011. [cited on pp. 5, 12, 41, 55]

[39] Brakemann, T. et al. **A reversibly photoswitchable GFP-like protein with fluorescence excitation decoupled from switching**. *Nat. Biotech.*, **29**(10):942–947, October 2011. [cited on p. 5]

[40] Grotjohann, T., Testa, I., Reuss, M., Brakemann, T., Eggeling, C., Hell, S.W. and Jakobs, S. **rsEGFP2 enables fast RESOLFT nanoscopy of living cells**. *eLife*, **1**, December 2012. [cited on pp. 5, 41, 55]

[41] Schwentker, M.A., Bock, H., Hofmann, M., Jakobs, S., Bewersdorf, J., Eggeling, C. and Hell, S.W. **Wide-field subdiffraction RESOLFT microscopy using fluorescent protein photoswitching**. *Microsc. Res. Techniq.*, **70**(3):269–280, 2007. [cited on p. 5]

[42] Rego, E.H., Shao, L., Macklin, J.J., Winoto, L., Johansson, G.A., Kamps-Hughes, N., Davidson, M.W. and Gustafsson, M.G.L. **Nonlinear structured-illumination microscopy with a photoswitchable protein reveals cellular structures at 50-nm resolution**. *PNAS*, **109**(3):E135–E143, January 2012. [cited on pp. 5, 55]

[43] Chmyrov, A., Keller, J., Grotjohann, T., Ratz, M., d'Este, E., Jakobs, S., Eggeling, C. and Hell, S.W. **Nanoscopy with more than 100,000 'doughnuts'**. *Nat. Methods*, **10**(8):737–740, August 2013. [cited on pp. 5, 12, 37, 55]

[44] Gustafsson, M.G.L. **Nonlinear structured-illumination microscopy: Wide-field fluorescence imaging with theoretically unlimited resolution**. *PNAS*, **102**(37):13081–13086, September 2005. [cited on p. 5]

[45] Bingen, P., Reuss, M., Engelhardt, J. and Hell, S.W. **Parallelized STED fluorescence nanoscopy**. *Opt. Express*, **19**(24):23716–23726, November 2011. [cited on p. 5]

[46] Yang, B., Przybilla, F., Mestre, M., Trebbia, J.B. and Lounis, B. **Massive Parallelization of STED Nanoscopy Using Optical Lattices**. arXiv e-print 1307.3833, July 2013. [cited on p. 5]

[47] Testa, I., Urban, N.T., Jakobs, S., Eggeling, C., Willig, K.I. and Hell, S.W. **Nanoscopy of Living Brain Slices with Low Light Levels**. *Neuron*, **75**(6):992–1000, September 2012. [cited on pp. 5, 48, 52, 57]

[48] Im, K.B., Han, S., Park, H., Kim, D. and Kim, B.M. **Simple high-speed confocal line-scanning microscope**. *Opt. Express*, **13**(13):5151–5156, June 2005. [cited on p. 6]

[49] Wolleschensky, R., Kempe, M. and Zimmermann, B. **High-speed confocal fluorescence imaging with a novel line scanning microscope**. *J. Biomed. Opt*, **11**(6):064011–064011–14, 2006. [cited on pp.]

[50] Mei, E., Fomitchov, P., Graves, R. and Campion, M. **A line scanning confocal fluorescent microscope using a CMOS rolling shutter as an adjustable aperture**. *J. Microsc.*, **247**(3):269–276, 2012. [cited on p. 6]

[51] Nyquist, H. **Certain Topics in Telegraph Transmission Theory**. *Trans. AIEE*, **47**(2):617–644, 1928. [cited on pp. 6, 39]

[52] Swift, D. **Image rotation devices — a comparative survey**. *Opt. Laser Technol.*, **4**(4):175–188, August 1972. [cited on p. 20]

[53] Hildebrand, R.H. **Focal Plane Optics In Far-Infrared And Submillimeter Astronomy**. *Opt. Eng.*, **25**(2):252323–252323–, 1986. [cited on p. 20]

[54] Moreno, I. **Jones Matrix for Image-Rotation Prisms**. *Appl. Opt.*, **43**(17):3373–3381, June 2004. [cited on p. 20]

[55] Hofferbert, R. et al. **LINC-NIRVANA for the large binocular telescope: setting up the world's largest near infrared binoculars for astronomy**. *Opt. Eng.*, **52**(8):081602–081602, 2013. [cited on p. 21]

[56] Beyer, W.H. *CRC Standard Mathematical Tables*. CRC Press, Boca Raton, 28th edition, 1987. page 220. [cited on p. 23]

[57] Denk, W., Strickler, J.H. and Webb, W.W. **Two-photon laser scanning fluorescence microscopy**. *Science*, **248**(4951):73–76, April 1990. [cited on p. 27]

[58] Helmchen, F. and Denk, W. **Deep tissue two-photon microscopy**. *Nat. Methods*, **2**(12):932–940, December 2005. [cited on pp. 27, 58]

[59] Hell, S. and Stelzer, E.H.K. **Fundamental improvement of resolution with a 4Pi-confocal fluorescence microscope using two-photon excitation**. *Opt. Commun.*, **93**(5–6):277–282, October 1992. [cited on p. 27]

[60] Axelrod, D. **Cell-substrate contacts illuminated by total internal reflection fluorescence**. *J. Cell. Biol.*, **89**(1):141–145, April 1981. [cited on p. 27]

[61] Axelrod, D. **Total Internal Reflection Fluorescence Microscopy in Cell Biology**. *Traffic*, **2**(11):764–774, 2001. [cited on p. 27]

[62] Huisken, J., Swoger, J., Bene, F.D., Wittbrodt, J. and Stelzer, E.H.K. **Optical Sectioning Deep Inside Live Embryos by Selective Plane Illumination Microscopy**. *Science*, **305**(5686):1007–1009, August 2004. [cited on p. 27]

[63] Poher, V., Kennedy, G.T., Manning, H.B., Owen, D.M., Zhang, H.X., Gu, E., Dawson, M.D., French, P.M.W. and Neil, M.A.A. **Improved sectioning in a slit scanning confocal microscope**. *Opt. Lett.*, **33**(16):1813–1815, August 2008. [cited on pp. 27, 32]

[64] Alda, J. **Laser and Gaussian Beam Propagation and Transformation**. In *Encyclopedia of Optical Engineering*, pages 999–1013. Marcel Dekker, Inc., 2003. [cited on p. 28]

[65] Harke, B., Keller, J., Ullal, C.K., Westphal, V., Schönle, A. and Hell, S.W. **Resolution scaling in STED microscopy**. *Opt. Express*, **16**(6):4154–4162, March 2008. [cited on p. 36]

[66] Ober, R.J., Ram, S. and Ward, E.S. **Localization Accuracy in Single-Molecule Microscopy**. *Biophys. J.*, **86**(2):1185–1200, February 2004. [cited on p. 42]

[67] Richardson, W.H. **Bayesian-Based Iterative Method of Image Restoration**. *J. Opt. Soc. Am.*, **62**(1):55–59, January 1972. [cited on p. 43]

[68] Lucy, L.B. **An iterative technique for the rectification of observed distributions**. *Astronomical Journal*, **79**:745, June 1974. [cited on p. 43]

[69] Yaroslavsky, L.P. and Caulfield, H.J. **Deconvolution of multiple images of the same object**. *Appl. Opt.*, **33**(11):2157–2162, April 1994. [cited on p. 43]

[70] Verveer, P.J. and Jovin, T.M. **Improved Restoration from Multiple Images of a Single Object: Application to Fluorescence Microscopy**. *Appl. Opt.*, **37**(26):6240–6246, September 1998. [cited on p. 43]

[71] Carrington, W. **Imaging Live Cells in 3D Using Wide-Field Microscopy with Image Restoration**. In Diaspro, A., editor, *Confocal and Two-Photon Microscopy: Foundations, Applications, and Advances*, page 337. John Wiley & Sons, Inc., 2001. [cited on p. 43]

[72] Vicidomini, G., Boccacci, P., Diaspro, A. and Bertero, M. **Application of the split-gradient method to 3D image deconvolution in fluorescence microscopy**. *J. Microsc.*, **234**(1):47–61, 2009. [cited on p. 44]

[73] Carrington, W.A., Lynch, R.M., Moore, E.D., Isenberg, G., Fogarty, K.E. and Fay, F.S. **Superresolution three-dimensional images of fluorescence in cells with minimal light exposure**. *Science*, **268**(5216):1483–1487, June 1995. [cited on p. 44]

[74] Kano, H., Voort, H.T.M.v.d., Schrader, M., Kempen, G.M.P.v. and Hell, S.W. **Avalanche photodiode detection with object scanning and image restoration provides 2–4 fold resolution increase in two-photon fluorescence microscopy**. *Bioimaging*, **4**(3):187–197, 1996. [cited on p. 44]

[75] Jonkman, J.E.N. and Stelzer, E.H.K. **Resolution and Contrast in Confocal and Two-Photon Microscopy**. In Diaspro, A., editor, *Confocal and Two-Photon Microscopy: Foundations, Applications, and Advances*, page 108. John Wiley & Sons, Inc., 2001. [cited on p. 44]

[76] Hecht, E. *Optics*. Addison-Wesley, Reading, Mass., 2002. page 465. [cited on p. 44]

[77] Yuste, R. *Dendritic spines*. MIT Press, Cambridge, Mass., 2010. [cited on p. 47]

[78] Harris, K.M. and Kater, S.B. **Dendritic Spines: Cellular Specializations Imparting Both Stability and Flexibility to Synaptic Function**. *Annu. Rev. Neurosci.*, **17**(1):341–371, 1994. [cited on p. 48]

[79] Izeddin, I., Specht, C.G., Lelek, M., Darzacq, X., Triller, A., Zimmer, C. and Dahan, M. **Super-Resolution Dynamic Imaging of Dendritic Spines Using a Low-Affinity Photoconvertible Actin Probe**. *PLoS ONE*, **6**(1):e15611, January 2011. [cited on pp. 48, 52]

[80] Wu, G.Y., Deisseroth, K. and Tsien, R.W. **Spaced stimuli stabilize MAPK pathway activation and its effects on dendritic morphology**. *Nat. Neurosci.*, **4**(2):151–158, February 2001. [cited on p. 50]

[81] Hu, X., Viesselmann, C., Nam, S., Merriam, E. and Dent, E.W. **Activity-Dependent Dynamic Microtubule Invasion of Dendritic Spines**. *J. Neurosci.*, **28**(49):13094–13105, December 2008. [cited on p. 50]

[82] Urban, N.T., Willig, K.I., Hell, S.W. and Nägerl, U.V. **STED Nanoscopy of Actin Dynamics in Synapses Deep Inside Living Brain Slices**. *Biophys. J.*, **101**(5):1277–1284, September 2011. [cited on pp. 52, 57]

[83] Egner, A. and Hell, S.W. **Aberrations in Confocal and Multi-Photon Fluorescence Microscopy Induced by Refractive Index Mismatch**. In Pawley, J.B., editor, *Handbook Of Biological Confocal Microscopy*, pages 404–413. Springer US, January 2006. [cited on p. 52]

[84] Booth, M.J., Neil, M.A.A., Juskaitis, R. and Wilson, T. **Adaptive aberration correction in a confocal microscope**. *PNAS*, **99**(9):5788–5792, April 2002. [cited on p. 57]

[85] Ji, N., Milkie, D.E. and Betzig, E. **Adaptive optics via pupil segmentation for high-resolution imaging in biological tissues**. *Nat. Methods*, **7**(2):141–147, February 2010. [cited on p. 57]

[86] Vicidomini, G., Moneron, G., Han, K.Y., Westphal, V., Ta, H., Reuss, M., Engelhardt, J., Eggeling, C. and Hell, S.W. **Sharper low-power STED nanoscopy by time gating**. *Nat. Methods*, **8**(7):571–573, July 2011. [cited on p. 58]

[87] Vicidomini, G., Schönle, A., Ta, H., Han, K.Y., Moneron, G., Eggeling, C. and Hell, S.W. **STED Nanoscopy with Time-Gated Detection: Theoretical and Experimental Aspects**. *PLoS ONE*, **8**(1):e54421, January 2013. [cited on p. 58]

Abbreviations

1d	one direction
AFM	atomic force microscopy
DD	differential detection
FOV	field of view
FWHM	full width half maximum
IPR	infinite plane response
MTF	modulation transfer function
NA	numerical aperture
NSOM	near-field scanning optical microscopy
OTF	optical transfer function
PALM	photoactivated localization microscopy
PSD	position sensitive diode
PSF	point spread function
RESOLFT	reversible saturable optical fluorescence transitions
rsFP	reversible switchable fluorescent protein
sCMOS	scientific complementary metal-oxide semiconductor
SIM	structured illumination microscopy
SLM	spatial light modulator
SNR	signal to noise ratio
SSIM	saturated structured illumination microscopy
STED	stimulated emission depletion
STORM	stochastic optical reconstruction microscopy

ABBREVIATIONS

List of Figures

LIST OF FIGURES

Acknowledgements

This work was carried out at the Department of NanoBiophotonics at the Max Planck Institute for Biophysical Chemistry in Göttingen, Germany.

First, I would like to thank Prof. Stefan Hell, head of the department, for supervising my thesis and giving me the opportunity to work in a scientifically outstanding and highly stimulating interdisciplinary environment.

Prof. Michael Hausmann (Kirchhoff-Institute for Physics, Ruperto-Carola University Heidelberg) I would like to thank for his interest in my work and for taking the time to examine the thesis.

Furthermore I am especially thankful to:

Volker Westphal for contributing with invaluable advice to the success of this work, especially by sharing his ideas regarding the differential detection, and for assisting in the implementation of the K-mirror.

Jan Keller-Findeisen for his outstanding help with data analysis and countless stimulating discussions on microscopy related topics.

Nicolai Urban for enabling the imaging of dendritic spines. His excellent preparation of the brain slices contributed greatly to the success of the presented measurements.

Jaydev Jethwa for tremendous support, technical assistance and valuable advice; including all sorts of help with electronic and optic equipment, and his assistance for the alignment and maintenance of various laser systems.

Tim Grotjohann for sharing his expert knowledge of switchable proteins and many other kinds of biology related topics and for supporting the live-cell measurements.

Tanja Gilat and Ellen Rothermel for their excellent assistance with cell culture.

Andreas Schönle for help with data acquisition and providing the software Imspector.

The mechanical and optical workshop for their services.

Andriy Chmyrov and Rainer Pick for the design of the K-mirror.

Alf Honigmann for the preparation of supported lipid bilayers.

For critically proof-reading I am deeply thankful to Débora Machado Andrade, Jaydev Jethwa, Nicolai Urban, Jan Keller-Findeisen, Tim Grotjohann and Volker Westphal.

Finally, for many fruitful discussions and constant support I would like to thank Débora Machado Andrade, Mina Lee, Ilaria Testa, Chaintanya Ullal, Haisen Ta, Elisa D'Este, Sebastian Berning, Tanja Brakemann, Gael Moneron, Marcel Leutenegger, Christian Eggeling, Johanna Bückers, Daniel Jans, Martin Andresen, Veronika Mueller, Francisco Balzarotti, Stefan Jakobs, Jakob Bierwagen, Andreas Hüper and all former and current members of the department.